

POLITECNICO DI TORINO

Collegio di Ingegneria Meccanica

**Corso di Laurea Magistrale
in Ingegneria Meccanica**

Tesi di Laurea Magistrale

**CFD SIMULATION OF COMBUSTION
AND WATER INJECTION IN A GAS
TURBINE BURNER**



Relatori

Prof. Mirko Baratta
Prof.ssa Daniela Misul
Prof. Simone Salvadori
Dott. Ing. Prashant Goel

Candidato

Felice Perrupato

April 2021

ABSTRACT

Heavy duty gas turbines are one of the most used technologies for the power generation. Nowadays has been crucial, especially for the power generation sector, to comply a new sustainable development.

The main objective of this thesis is to define a 3D CFD water injection model optimizing the computational costs required by this kind of simulation.

Water injection strategy represent an answer to decrease the NO_x emissions produced by a heavy-duty gas turbine. The water inside the combustor works as a heat sink, lowering the temperature of the flame with the direct consequence on the NO_x abatement. Also, the water introduced is an additional working fluid inside the combustor and that produce a turbine power output increase.

The main cost to pay by introducing water inside the combustor is an overall efficiency decrease.

There are many possibilities to simulate the water injection inside the combustor of a gas turbine. The first one is represented by the VOF (Volume of Fluid) simulation, the second one by modelling the spray using ELSA spray atomization strategy.

In this work, to avoid the computational effort required by these two strategies, a study of water injection as a simple heat sink is proposed.

A first preliminary study on the NASA LDI gas turbine has been conducted to study how the ELSA spray atomization works and to have the reference to reproduce the water injection as a boundary condition.

From this analysis, the water injection study has been moved on the TG - 20 gas turbine real combustor with a process of optimization concerning the concentration of water and the influence of this boundary condition on the primary recirculation zone.

The model has been validate comparing the results in terms of NO_x, UHC, CO coming from experimental results.

Index

| | |
|---|----|
| 1. Introduction | 1 |
| 1.1 Motivation | 1 |
| 1.2 Thesis overview | 2 |
| 2. Gas turbines | 3 |
| 2.1 Combustor design | 4 |
| 2.1.1 Combustor types | 4 |
| 2.1.2 Diffuser | 5 |
| 2.1.3 Combustion zones | 6 |
| 2.1.4 Gas injection | 7 |
| 2.1.5 Wall cooling | 7 |
| 3. Theoretical preliminaries | 9 |
| 3.1 Governing equation | 9 |
| 3.1.1 General conservation equations | 9 |
| 3.1.2 Thermal and caloric equation of state | 10 |
| 3.1.3 Transport models | 11 |
| 3.2 Combustion chemistry | 13 |
| 3.3 Turbulence modelling | 15 |
| 3.3.1 Governing equations in RANS | 17 |
| 3.3.2 Eddy viscosity model | 18 |
| 3.3.3 RNG k- ϵ model | 19 |
| 4. Emissions | 22 |
| 4.1 Carbon Monoxide | 22 |
| 4.2 Oxides of Nitrogen | 23 |
| 4.2.1 Thermal Nitric Oxide | 24 |
| 4.2.2 Nitrous oxide Mechanism | 26 |
| 4.2.3 Prompt Nitric Oxide | 27 |
| 4.2.4 Fuel Nitric Oxide | 27 |
| 4.2.5 Influence of Pressure on Oxides of Nitrogen Formation | 27 |
| 4.3 Water injection | 28 |
| 5. Computational methods for fluid dynamics | 29 |
| 5.1 Finite volume methods | 30 |
| 5.1.1 PISO algorithm | 31 |

| | | |
|-------|---|----|
| 5.1.2 | Solution procedure | 32 |
| 5.1.3 | MUSCL | 33 |
| 5.2 | Mesh generation | 33 |
| 5.2.1 | Grid scaling | 33 |
| 5.2.2 | Fixed embedding | 34 |
| 5.2.3 | Adaptive mesh refinement (AMR)..... | 34 |
| 6. | TG – 20 model, case setup and results | 37 |
| 6.1 | TG – 20 geometry model..... | 37 |
| 6.2 | Dry Case | 39 |
| 6.3 | Preliminary study..... | 49 |
| 7. | Conclusions and future directions | 52 |
| 8. | Figure index..... | 53 |
| 9. | Bibliography..... | 55 |

1. Introduction

1.1 Motivation

The worldwide power demand is increasing year by year, for this reason the power plant used for the energy production are under investigation to comply a certain sustainability.

The industrial gas turbine play an important role in the production of the electrical energy and for this reason become mandatory to study the pollutant emissions produced by this plant and to find new strategy to reduce those emissions.

Even if the pandemic decreases the power demand, it does not affect the growing trend as showed in Figure 1.1 provided by the IEA (International Energy Agency). [1]

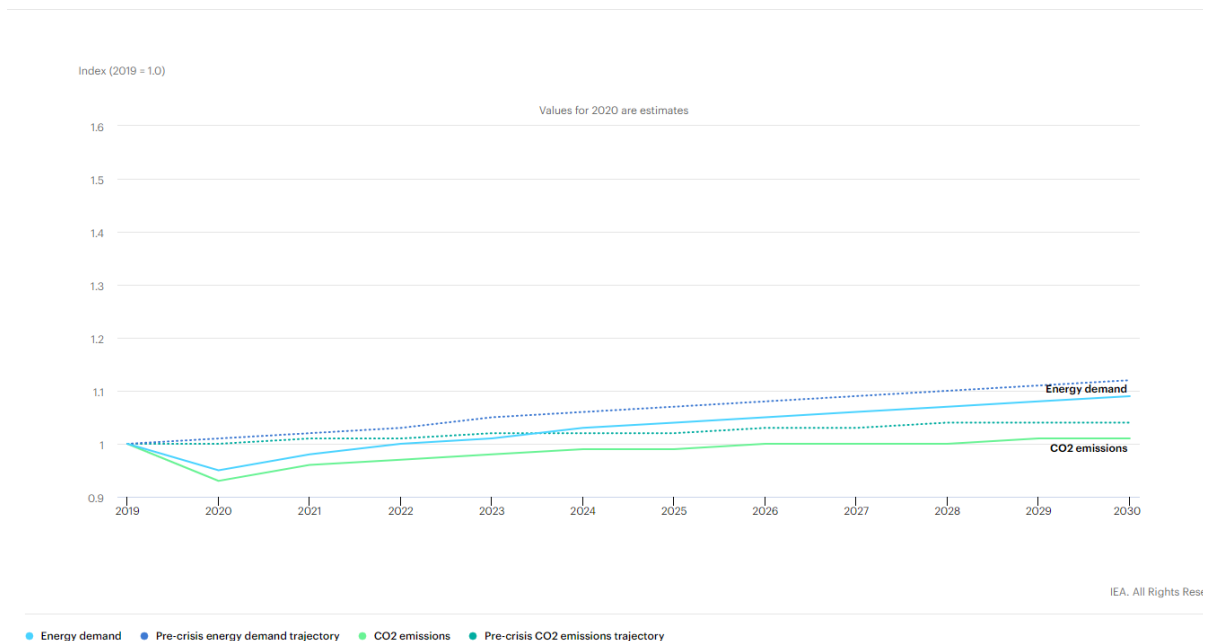


Figure 1.1 Global energy demand and CO2 emissions trends in the Stated Policies Scenario, 2019-2030

The industrial gas turbine play an important role in the production of the electrical energy and for this reason become mandatory to study the pollutant emissions produced by this plant and to find new strategy to reduce those emissions.

The pollutants that the combustion of a gas turbine alimeted by natural gas produce are CO₂, CO, NO_x and UHC.

NO_x emissions are directly correlated to the flame temperature, due to the thermal formation mechanism.

Water injection can be a response to lower the NO_x level. In fact, the heats subtracted to evaporate the water in the primary zone of the gas turbine combustor has the main effect to lower the flame temperature.

To optimize the water injection strategy inside the combustor, experimental studies can be too much expensive in terms of time and costs.

For this reason and thanks to increasing in computing performance, the numerical simulation of the combustion can be a powerful instrument to analyse this phenomenon, avoiding all the difficulties coming from an experimental campaign.

In this work, the Computational Fluid Dynamics to simulate the combustion is applied using the finite volume method. The software used for the numerical modelling is CONVERGE.

The objective is to propose a simplified heat model to reproduce the heat subtraction in the primary zone due by the water evaporation.

The turbulence model adopted is the RNG RANS model, computational less expensive than LES or DNS but also accurate for this study. The FGM strategy with two different reaction mechanism has been used to model the combustion.

A first study on a dry model has been conducted using two different reaction mechanism, the GRI mechanism and more detailed CRECK mechanism, implementing an enhanced wall treatment and a second order spatial method for the convective term with the aim to improve the accuracy of the model.

A simplified geometry, the NASA LDI combustor, has been taken in consideration to conduct a preliminary study on the heat sink by comparing the model with the water injection. Three different evaporation model are taken in consideration and the results suggest that the water modelled as simple heat sink can be accurate enough. The model presents a geometric similitude with the combustor of the TG – 20.

Starting from this preliminary study, the model can be implemented and optimized on the real combustor of the TG – 20.

1.2 Thesis overview

Chapter 1: Thesis introduction and motivation of the work

Chapter 2: Gas turbine description, Joule Brayton thermodynamic cycle and an overview of the combustor geometry and design

Chapter 3: Governing equation used in numerical model of turbulent combustion.

Chapter 4: Pollutant emission formation mechanism and water injection strategy to reduce the NO_x emissions.

Chapter 5: CFD working principles: finite volume method, PISO algorithm and mesh generation.

Chapter 6: 3D geometry model, main results coming from simulation and preliminary study on the NASA LDI combustor.

2. Gas turbines

A gas turbine is a turbomachinery that convert the energy provided by a gaseous or liquid fuel into mechanical energy.

In an industrial gas turbine, this energy will drive a power generator producing electrical energy. The energy is usually obtained by expansion through a turbine. Here the air expands with a certain pressure ratio, so the air must be firstly compressed. In a single-shaft gas turbine the turbine drives the compressor using the same shaft.

Before the turbine, the energy of the fluid is increased by combustion that occurs in a combustor. The fuel taking in account that the energy of the combustion must be necessary to drive the compressor and to produce a power output.

The Joule-Brayton cycle (Figure 2.1) is the reference to describe the thermodynamics evolution of the fluid in a gas turbine, described above.

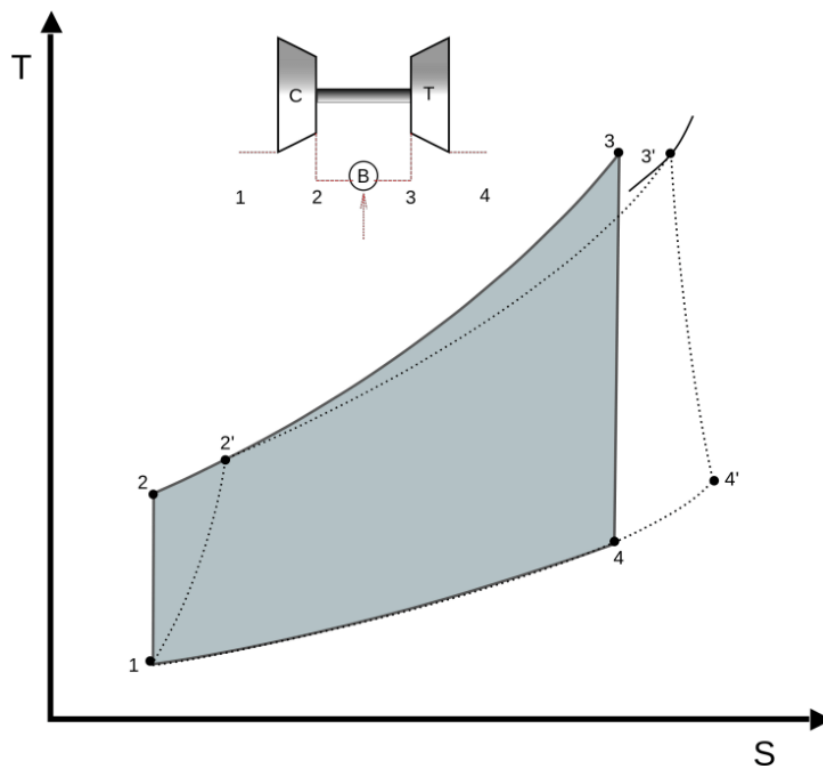


Figure 2.1 T-S diagram of a Joule-Brayton cycle [2]

The solid line is the ideal working cycle, the dashed the real one. There are several reasons why the real and ideal cycle differ.

- The real expansion and compression are not reversible and not adiabatic.
- Pneumatic losses take place inside the burner.
- High temperature at the end of combustion lead to heat losses for dissociation.
- The combustion is not complete.

2.1 Combustor design

Several are the variations on a gas turbine combustor design, but the main structure is always almost the same including an air casing, diffuser, liner, fuel injector.

A combustor must satisfy some basic requirements like as:

- High combustion efficiency
- Reliable and smooth ignition
- Wide stability limits
- Low pressure loss
- An outlet temperature distribution that is studied taking in account the limit in temperature of the turbine blades
- Low emissions of smoke and gaseous pollutant species
- Freedom from pressure pulsations and other manifestations of combustion-induced instability
- Size and shape compatible with engine envelope
- Design for minimum cost and ease of manufacturing
- Maintainability
- Durability
- Multi-fuel capability

Industrial engine requires a long operating life and multifuel capability, low fuel consumption and low pollutant emissions [3].

2.1.1 Combustor types

Combustor type choice is related to the overall engine design and by the need to use available space as effectively as possible.

Two main types of combustor can be mentioned: “tubular” and “annular”. A third type, the “tuboannular” or “can-annular”, is a compromise between these one.

The

Figure 2.2 shows the three different combustor types:

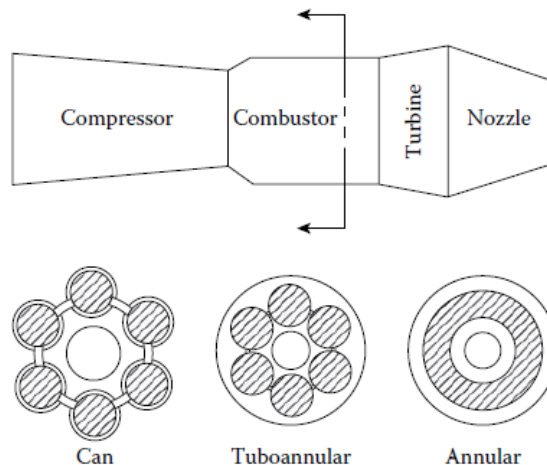


Figure 2.2 The three main combustor types [3]

Tubular combustor is made by a cylindrical liner mounted concentrically inside a cylindrical casing. Its development requires little time and low cost. On the other side, their length and weight are prohibitive for aircraft engines and so, their application is mainly related to industrial field also considering the easy accessibility and maintenance.

Annular combustor consists in an annular liner mounted concentrically inside an annular casing. Its clean aerodynamic layout results in a compact unit that imply a lower pressure loss than the other combustor types. The main issue is given by the heavy buckling load on the outer line so, annular lines are confined to engines of low-pressure ratio. Also, a very high cost is required to supply air at the levels of pressure, temperature and flow rate needed to test large annular combustion chamber at full-load conditions.

Tuboannular presents a group of tubular liners arranged inside a single annular casing combining the compactness of annular chamber with the mechanical strength of tubular. Compared to the annular, the air supply is very modest. The main drawback is to achieve a satisfying airflow pattern and design the diffuser can be very difficult [3].

2.1.2 Diffuser

A fundamental requirement is to minimize the pressure drop across the combustor. A part of the pressure drop occurs the air is simply pushed inside the combustor, the other when heat is added to a high-velocity stream.

The first one, that can be called “cold loss”, is the sum of the losses in the diffuser and in the liner. From a combustion point of view, the pressure drop inside the diffuser is totally lost, whereas the liner loss develops as turbulence, with all the benefits in terms of mixing for the combustion. Ideally, a combustor would present a total cold pressure loss in the liner.

The pressure loss due to heat adding to the flow, can be written as a function of the inlet temperature T_3 and the outlet temperature T_4 :

$$\Delta P_{\text{hot}} = 0.5\rho u^2 \left[\frac{T_4}{T_3} - 1 \right] \quad (2.1)$$

The diffuser reduces the compressor outlet velocity u . In this way, a tolerable pressure drop value is achieved. Also, the diffuser recovers as much of the dynamic pressure as possible. In so doing, the flow at the liner will be smooth and stable.

There two main type of diffuser design. The first one consists in a long aerodynamic diffuser located near the compressor outlet. This diffuser achieves a reduction in velocity about 35%, before the air reaches the snout in which the flows is divided into three separate diffusing passages. Two passages convey the air to the inner and outer liner annuli in equal proportion. The central diffuser passage discharges the air into the dome region, providing air for atomization and dome cooling.

The other one is called “dump” or “step” diffuser. The inlet air velocity is halved by this diffuser. At the exit, the air is then “dumped” and left to divide itself between air for the inner and outer annuli and dome air.

Figure 2.3 shows the design type of diffuser.

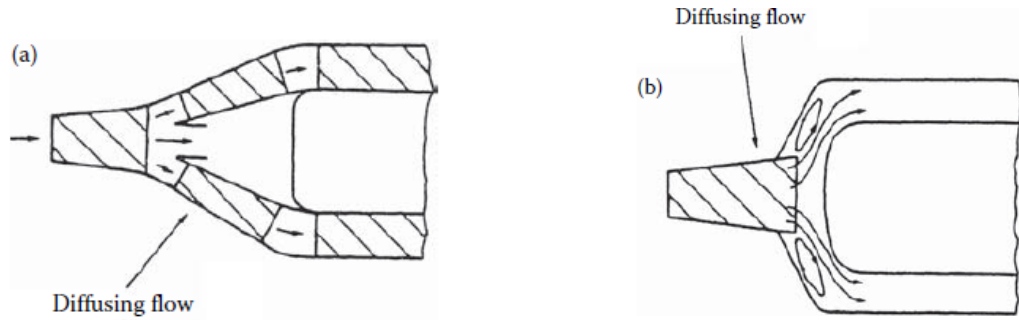


Figure 2.3 Two basic types of annular diffusers: (a) aerodynamic, (b) dump. [3]

2.1.3 Combustion zones

The combustor can be divided in three zones where the combustion occurs:

- Primary zone
- Intermediate zone
- Dilution zone

Primary zone provides to the flame the temperature, time and turbulence needed to achieve a complete combustion of the working fluid. In this zone a toroidal flow reversal is common and recirculates a portion of hot combustion gases in order to have a continuous ignition to the incoming mixture.

Intermediate zone due to dissociation that occurs in primary zone where the temperature reaches 2000K, the concentration of CO and H₂ is significant in the flux. So, in this zone an amount of air is added to oxidize soot and allows the combustion of CO and other unburned hydrocarbons (UHC).

Dilution zone the air not needed for combustion and wall cooling (usually between the 20% and 40 % of the total) is admitted in this zone, in order to have an allowable temperature distribution to the turbine. This temperature distribution is defined as “pattern factor” or “temperature traverse quality”. The air is introduced through one or more rows of holes in the liner walls. Their shape and size are selected to optimize the penetration of air jets and, thus, the mixing with the main stream [3].

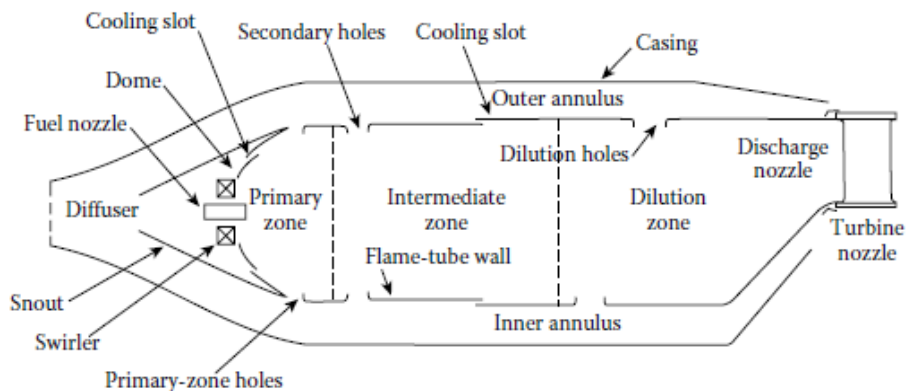


Figure 2.4 Main components of a conventional combustor [3]

2.1.4 Gas injection

To inject gaseous fuels the methods used are a plain orifices and slots, swirlers and venturi nozzles.

Natural gases present few problems from a combustion point of view.

The main problem is to reach the required mixing rate in the combustion zone. A too high mixing rate leads to a poor lean-blowout characteristic, on the other side a too low could give rise to rough combustion. [3]

2.1.5 Wall cooling

The liner main function is to contain the combustion process and to distribute the air to the combustion zones. For this reason, it must be structurally strong to withstand the buckling load due to pressure differential across the liner wall. Another important feature is the thermal resistance to withstand the continuous and cyclic high-temperature operation.

So, the materials used for the liner must be oxidant and high temperature resistant, also an effective use of cooling air is mandatory.

More than the 20% of air of the total air mass flow is used to cool the liner wall.

The temperature of the liner is the results of the balance between the heat received by radiation and convection from the hot gas and the heat transferred from it by convection to the annulus air and by radiation to the air casing.

Pressure ratio increasing can also be problematic. In fact, a raise in pressure ratio means an increase of the inlet air temperature. This raise in temperature has two main effect: an increase of the flame temperature that increase the heat transferred to the liner wall and a reduction of the cooling effectiveness of the air. [3]

3. Theoretical preliminaries

A description of fluid flow and chemistry phenomena that are involved in the combustion is presented.

To have a complete view of these processes, it is necessary to model all these phenomena using a system of partial differential equation.

3.1 Governing equation

3.1.1 General conservation equations

The mass conservation equation can be expressed using the continuity:

$$\frac{\partial \rho}{\partial t} + \nabla \cdot (\rho \mathbf{u}) = 0 \quad (3.1)$$

The quantities involved in this equation are the density of the mixture ρ , \mathbf{u} three-dimensional vector and t the time.

The momentum conservation equation can be described by the Navier-Stokes's equation [4]

$$\frac{\partial(\rho \mathbf{u})}{\partial t} + \nabla \cdot (\rho \mathbf{u} \mathbf{u}) + \nabla \cdot (\boldsymbol{\tau}) + \nabla p - \rho \mathbf{g} = 0 \quad (3.2)$$

Where vector \mathbf{g} is the gravitational acceleration field, $\boldsymbol{\tau}$ the stress tensor and p the pressure.

Introducing the enthalpy h and internal energy e it is possible to obtain the energy conservation equation, expressed by

$$\frac{\partial(\rho h)}{\partial t} + \nabla \cdot (\rho \mathbf{u} h) + \nabla \cdot (q) + \boldsymbol{\tau} : \nabla \mathbf{u} - \frac{D(p)}{Dt} = 0 \quad (3.3)$$

Indicating with q the heat flux. The equation contains on the left-hand side the enthalpy production due to viscous dissipation and pressure variations.

For combustion application it is usual to neglect the effect of viscous term.

The variation in composition is expressed by the conservation equation of the chemical species:

$$\frac{\partial \rho_i}{\partial t} + \nabla \cdot (\rho_i \mathbf{u}_i) = \dot{w}_i \quad i \in [1, N_s] \quad (3.4)$$

In this a source \dot{w}_i representing the formation and destruction by chemical reactions is taken account. The other terms are ρ_i the mass density of species i , \mathbf{u}_i the velocity of species and N_s the total number of species.

The total amount of mass must be conserved, so

$$\sum_{i=1}^{N_s} \dot{w}_i = 0 \quad (3.5)$$

From the definition of species mass fraction Y_i

$$Y_i = \frac{\rho_i}{\rho} \quad (3.6)$$

And writing the velocity of the species as

$$\mathbf{u}_i = \mathbf{u} + \mathbf{U}_i \quad (3.7)$$

With \mathbf{U}_i is defined as the diffusion velocity of the species, that is the deviation from the bulk flow velocity \mathbf{u} , can be derived another form of the equation (3.4)

$$\frac{\partial(\rho Y_i)}{\partial t} + \nabla \cdot (\rho \mathbf{u} Y_i) = -\nabla \cdot (\rho \mathbf{U}_i Y_i) + \dot{w}_i \quad i \in [1, N_s] \quad (3.8)$$

It can be seen how the different physical effects are separated in the equation: the time dependency, convection, diffusion, and chemical production.

Applying the summation to the equation ??, the diffusion velocity goes to zero.

$$\sum_{i=1}^{N_s} Y_i \dot{w}_i = 0 \quad (3.9)$$

3.1.2 Thermal and caloric equation of state

The relation between pressure to density and temperature to the species mass fraction can be defined by the thermal equation of state.

Under the approximation of an ideal gas, the partial pressure is defined as [4]

$$p_i = n_i R^0 T \quad (3.10)$$

The terms involved in this equation are n_i the molar concentration of the species i , T the temperature of the mixture, R^0 .

The molar concentration is equal to

$$n_i = n \cdot X_i = \rho \frac{Y_i}{M_i} \quad (3.11)$$

With n the molar concentration of the total gas mixture, X_i the species mole fraction and M_i the molecular mass of the species i .

Is now possible to define the thermodynamic pressure p as:

$$p = \sum_{i=1}^{N_S} p_i = \sum_{i=1}^{N_S} \rho R^0 T \frac{Y_i}{M_i} \quad (3.12)$$

the caloric equation of state is also useful to define the species enthalpy h_i :

$$h_i = h^{ref} + \int_{T^{ref}}^T c_{p,i} T dT \quad (3.13)$$

So, the enthalpy of the species is given by two components: the enthalpy of formation h^{ref} at the temperature T^{ref} and the integral part, defined as the thermal enthalpy. $c_{p,i}$ represent the specific heat at constant pressure of each species.

Again, the summation overall the species enthalpies define the total enthalpy of the mixture:

$$h = \sum_{i=1}^{N_S} Y_i h_i \quad (3.14)$$

3.1.3 Transport models

Stokes law of friction model the viscous stress tensor under the hypothesis that the medium behaves like a single-component Newtonian fluid:

$$\boldsymbol{\tau} = \mu \left(\nabla \mathbf{u} + (\nabla \mathbf{u})^T - \frac{2}{3} (\nabla \cdot \mathbf{u}) \mathbf{I} \right) \quad (3.15)$$

Here μ is the dynamic viscosity of the mixture and \mathbf{I} is the unit tensor.

Using the Fick law equation is possible to write the diffusion velocity field \mathbf{U}_i :

$$\mathbf{U}_i = -\frac{D_i}{X_i} \nabla X_i \quad (3.16)$$

Where the coefficient D_i is the mixture-averaged diffusion.

The heat flux instead can be modelled by using the Fourier's Law:

$$q = \lambda \nabla T + \rho \sum_{i=1}^{Ns} h_i \nabla Y_i \left(\frac{1}{Le_i} - 1 \right) \quad (3.17)$$

Where λ is the thermal conductivity of the mixture.

The heat flux can be written introducing the enthalpy instead of temperature:

$$q = -\frac{\lambda}{c_p} \nabla h - \frac{\lambda}{c_p} \sum_{i=1}^{Ns} h_i \nabla Y_i \left(\frac{1}{Le_i} - 1 \right) \quad (3.18)$$

The Le_i is a dimensionless number, expressed as the ratio between the thermal and mass diffusivity of the species.

$$Le_i = \frac{\lambda}{c_p D_p} \quad (3.19)$$

Where can be recognized $\frac{\lambda}{c_p}$ as the thermal diffusivity and D_p the mass diffusivity. When this number is equal to one, mass and heat diffuses at the same rate in the flame, on the other side species and heat will locally distribute. For turbulent combustion, the Lewis number can be considered constant.

The dynamic viscosity can be written as a function of the mass fraction [4]:

$$\mu_i = \sum_{i=1}^{Ns} \frac{Y_i \mu_i}{M_i \left(\sum_{j=1}^{Ns} \frac{Y_j \Phi_{ij}}{M_{ij}} \right)} \quad (3.20)$$

And

$$\Phi_{ij} = \frac{1}{\sqrt{8}} \left(1 + \frac{M_i}{M_j} \right)^{-1/2} \left[1 + \left(\frac{\mu_i}{\mu_j} \right)^{1/2} \left(\frac{M_i}{M_j} \right)^{1/4} \right] \quad (3.21)$$

Also, the thermal conductivity and the mixture-averaged diffusion coefficient can be expressed as a function of the mass fraction:

$$\lambda = \frac{1}{2} \left[M \sum_{i=1}^{Ns} \frac{Y_i \lambda_i}{M_i} + \left(M \sum_{i=1}^{Ns} \frac{Y_i}{M_i \lambda_i} \right)^{-1} \right] \quad (3.22)$$

$$D_i = \frac{1 - Y_i}{M \sum_{j \neq i}^{Ns} \frac{Y_j}{M_j D_{ij}}} \quad (3.23)$$

Most of the CFD codes take in account a simplified formulation to reduce the computational cost of the transport coefficients calculation [4].

$$\frac{\partial(\rho h)}{\partial t} + \nabla \cdot (\rho \mathbf{u} h) \quad (3.24)$$

Finally, the heat flux vector expression can be substituted inside the conservation equations for enthalpy and species. The final equation is:

$$\frac{\partial(\rho h)}{\partial t} + \nabla \cdot (\rho \mathbf{u} h) = \nabla \cdot \left(\frac{\lambda}{c_p} \nabla h \right) + \nabla \cdot \frac{\lambda}{c_p} \sum_{i=1}^{Ns} h_i \nabla Y_i \left(\frac{1}{Le_i} - 1 \right) + \boldsymbol{\tau} : \nabla \mathbf{u} + \rho \mathbf{u} \cdot \mathbf{g} + \frac{d p}{d t} \quad (3.25)$$

$$\frac{\partial(\rho Y_i)}{\partial t} + \nabla \cdot (\rho \mathbf{u} Y_i) = \nabla \cdot \left(\frac{\lambda}{c_p Le_i} \nabla Y_i - 1 \right) + \dot{w}_i \quad (3.26)$$

It can be useful also to define the element mass fraction Z_j of the element j :

$$Z_j = \sum_{i=1}^{Ns} \left(\frac{a_{ji} M_j}{M_i} \right) Y_i = \sum_{i=1}^{Ns} w_{ji} Y_i \quad j \in [1, N_e] \quad (3.27)$$

Where N_e is the number of elements, w_{ji} the relative mass fraction, M_j the molar mass of element j , a_{ji} the number of atoms of j in species i .

The species conservation equation can now be written as

$$\frac{\partial(\rho Z_j)}{\partial t} + \nabla \cdot (\rho \mathbf{u} Z_j) = \nabla \cdot \left(\frac{\lambda}{c_p} \nabla Z_j \right) + \nabla \cdot \left(\frac{\lambda}{c_p} \sum_{i=1}^{Ns} \left(\frac{1}{Le_i} - 1 \right) w_{ji} \nabla Y_i \right) \quad (3.28)$$

3.2 Combustion chemistry

The combustion of methane with air is given by the global reaction:



This reaction is the result of a large sequence of a chain of elementary equations in which many radicals are involved. This series of reaction results in an exothermic reaction where the fuel is oxidized in products [4].

So, a reversible chemical reaction can be written as

$$\sum_{i=1}^{N_s} v'_{ij} A_i \rightleftharpoons \sum_{i=1}^{N_s} v''_{ij} A_i \quad j \in [1, N_r] \quad (3.30)$$

indicating with v'_{ij} and v''_{ij} the forward and backward molar reaction coefficients of species i in reaction j , N_r the number of elementary reactions and A_i the species i .

Is now possible to define the net chemical source term of species i [4]:

$$\dot{w}_i = M_i \sum_{j=1}^{N_r} (v''_{ij} - v'_{ij}) r_j \quad i \in [1, N_s] \quad (3.31)$$

Where r_j is the reaction rate for elementary reaction j , which is given by:

$$r_j = k_j^f \prod_{i=1}^{N_s} \left[\frac{\rho Y_i}{M_i} \right]^{v'_{ij}} - k_j^b \prod_{i=1}^{N_s} \left[\frac{\rho Y_i}{M_i} \right]^{v''_{ij}} \quad j \in [1, N_r] \quad (3.32)$$

the rate of formation and consumption, indicated with k in the previous equation, are given by the Arrhenius law [4]:

$$k_j = A_j T^{\beta_j} \exp\left(\frac{-E_{a,j}}{R^0 T}\right) \quad j \in [1, N_r] \quad (3.33)$$

3.3 Turbulence modelling

Turbulent fluid motion, that characterized most flows encountered in engineering practice, can be defined as an irregular motion in which various quantity show a random variation with time and space coordinates, so that statistically distinct average values can be discerned [5].

So, turbulent flows show the following properties:

- Turbulent flows are highly unsteady. Velocity as function of time at most points in the flow show a random shape.
- This kind of flows are three-dimensional. The time-averaged velocity may be a function of only two coordinates, but the instantaneous field fluctuates rapidly in three spatial dimensions.
- They contain a great deal of vorticity. Indeed, vortex stretching is one of the principal mechanisms by which the intensity of turbulence is increased.
- Turbulence increases the rate at which conserved quantities are stirred. Stirring is a process in which parcels of fluid with differing concentrations of at least one of the conserved properties are brought in contact. The actual mixing is accomplished by diffusion, and so the process can be called turbulent diffusion.
- By means of this process, turbulence brings fluids of differing momentum content into contact. The reduction of the velocity gradient due to the action of viscosity reduces the kinetic energy of the flow; so, mixing is a dissipative process. The lost of energy is irreversibly converted in internal energy of the fluid-
- Turbulent flows contain coherent structures: repeatable and essentially deterministic events that are responsible for a large part of mixing. However, the random component of turbulent flows causes these events to differ from each other in size, strength, and time interval between occurrences, making study of them very difficult.
- Turbulent flows fluctuate on a broad range of length and time scales. This property makes direct numerical simulation very difficult.

Turbulence produces some effects, not always desirable, depending on the application. In example when chemical mixing and heat transfer are needed, an intense mixing is useful. That leads to an increased mixing of momentum that results in an increased frictional force. As result, more power is needed to propel a vehicle.

In the past, turbulence has been studied mainly on the experimental side, requiring detailed measurement that are costly and time consuming.

For that reason, nowadays numerical methods have an important role. [6]

There are six categories to classify the approaches to predicting turbulent flows, according to Bardina [7]

- The first involves the use of correlations such as ones that give the friction factor as a function of the Reynolds number or the Nusselt number of heat transfer as function of the Reynolds and Prandtl numbers. This method is limited to simple types of flows that can be characterized by just few parameters.
- The second uses integral equations which can be derived from the equations of motion by integrating over one or more coordinates. Usually this reduces the problem to one or more ordinary differential equations which are easily solved. The methods applied to these equations are those for ordinary differential equations.
- The third is based on equations obtained by averaging the equations of motion over the time (when the flow is statistically steady), over a coordinate in which the mean flow

does not vary, or over an ensemble of realizations (an imaged sets if flows in which all controllable factors are kept fixed). This approach is called one-point closure and leads to a set of partial differential equations called the Reynolds-averaged Navier-Stokes (RANS) equations. These equations do not form a closed set, so this method requires the introduction of approximations (a turbulence model).

- The fourth type of method is called two-point closure. It uses equations for the correlation of the velocity components at two spatial points or, more often, the Fourier transform of these equations. These methods are rarely used except for homogeneous turbulence.
- The fifth is large eddy simulation (LES) and solves the large-scale motions of the flow while approximating or modelling only the small scale motions. It can be a compromise between one-point closure model and direct simulation.
- The last one is the direct numerical simulation (DNS) in which the Navier-Stokes equations are solved for all the motions in a turbulent flow

DNS is the most accurate method, allowing to compute statistical quantities that can be compared directly to the experimental data to validate the results. On the other hand, DNS usage is limited only to small scale academic problems, due to the computational cost required. LES approach reduces the computational cost of the simulation. The main difference lies on the range of the eddy sizes that the two methods take in consideration.

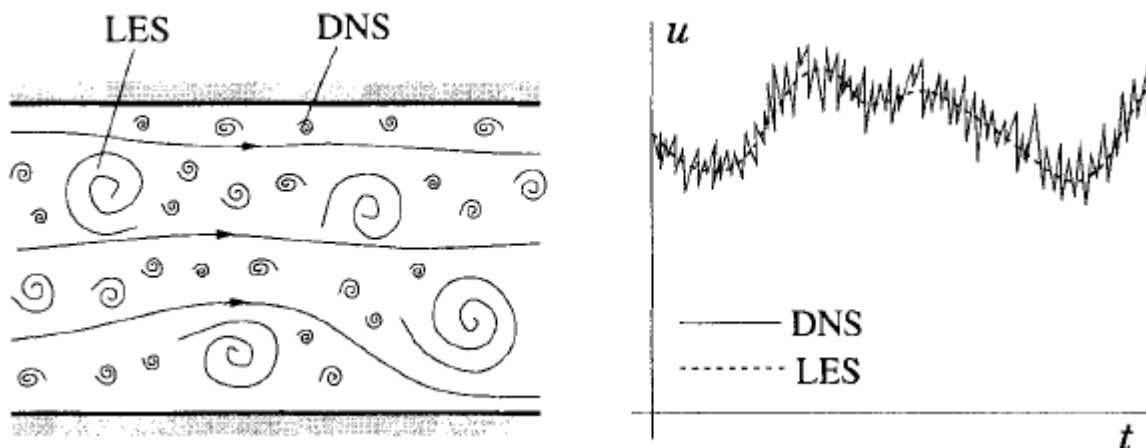


Figure 3.1 Schematic representation of a turbulent motion (left) and the time dependence of a velocity component at a point (right) [6]

LES methods consider that the large-scale motions are much more energetic than the small ones; for this reason, they are by far the most effective transporters of the conserved properties. So, a simulation that treats large eddies more exactly than the small one can be accurate enough for most of the problems encountered.

LES simulations are three-dimensional, time dependent and require a considerable computational effort, but much less expensive than the DNS, so it can be used when the Reynolds number is too high, or geometry is too complex to allow a DNS application.

The cost of the simulation required in a LES is reduced by filtering the velocity field. So, the resolved scale is a local average of the complete field.

Usually, few quantitative properties of a turbulent flow like the average forces on a body, the degree of mixing between two incoming streams of fluid or the amount of a substance that has

reacted are the main interest in a CFD analysis and using the methods described above to compute these quantities is not affordable and is like to overkill the problem.

Despite the less information provided, the RANS model can be the final compromise between computational cost and turbulence modelling. For this reason, this method is the one chosen.

In Reynolds-averaged approaches to turbulence, all the unsteadiness is averaged out.

In so doing, the non-linearity of the Navier-Stokes's equations gives rise to terms that must modelled.

Turbulence is a complex phenomenon, and this makes it unlikely that by single Reynolds-averaged model will be able to represent all turbulent flows so turbulence models should be regarded as engineering approximations.

3.3.1 Governing equations in RANS

When a statistically steady flow is considered, every variable can be written as the sum of a time-averaged value and a fluctuation about that value:

$$\phi(x_i, t) = \bar{\phi}(x_i) + \phi'(x_i, t) \quad (3.34)$$

Where the time-averaged $\bar{\phi}(x_i)$ value is defined as:

$$\bar{\phi}(x_i) = \lim_{T \rightarrow \infty} \frac{1}{T} \int_0^T \phi(x_i, t) dt \quad (3.35)$$

T is the averaging interval and t the time. The interval considered must be large compared to the typical time scale of the fluctuations; for this reason, $T \rightarrow \infty$ limit is considered, as seen in Figure 3.2.

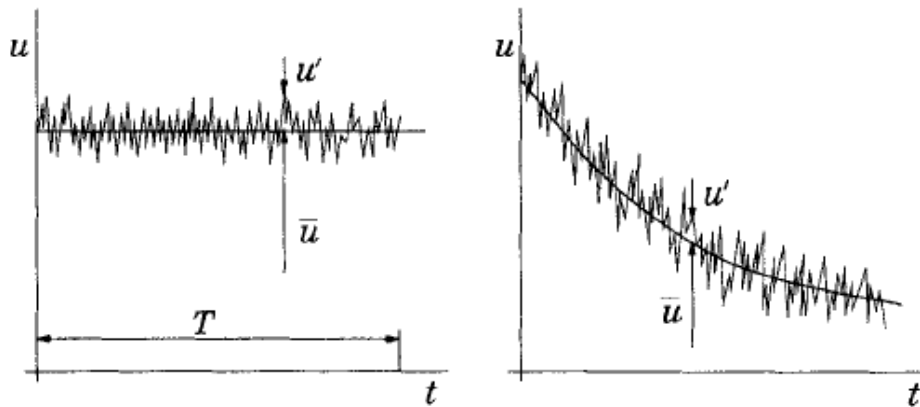


Figure 3.2 Time averaging for a statistically steady flow (left) and ensemble averaging [6]

If T is large enough, the time-averaged variable does not depend on the time in which the averaging is started.

An ensemble averaging must be operated when the flow is unsteady:

$$\bar{\phi}(x_i) = \lim_{N \rightarrow \infty} \frac{1}{N} \sum_{n=1}^N \phi(x_i, t) \quad (3.36)$$

Where N is the number of members of the ensemble and must be large enough to eliminate the effects of fluctuations and this approach can be applied to any flow. Applying the averaging process to the Navier-Stokes's equations leads to the RANS equations.

The average of a linear term in the conservation equations gives the identical term for the averaged quantity. From a quadratic nonlinear term, we get two terms, the product of the average and covariance:

$$\overline{u_i \phi} = \overline{(u_i + u'_i)(\phi + \phi')} = \overline{u_i \phi} + \overline{u'_i \phi'} \quad (3.37)$$

Two terms called Reynolds's tensor stress and turbulent scalar fluxes results from the average of conservation equations. These terms cannot be expressed as function of mean quantities.

Considering an incompressible flow, the averaged continuity and momentum equations can be written as:

$$\frac{\partial(\rho \bar{u}_i)}{\partial x_i} = 0 \quad (3.38)$$

$$\frac{\partial(\rho \bar{u}_i)}{\partial t} + \frac{\partial(\rho \bar{u}_i \bar{u}_j + \rho \bar{u}'_i \bar{u}'_j)}{\partial x_j} = - \frac{\partial \bar{p}}{\partial x_i} + \frac{\partial \bar{\tau}_{ij}}{\partial x_j} \quad (3.39)$$

Where the $\bar{\tau}_{ij}$ are the mean viscous stress tensor components:

$$\bar{\tau}_{ij} = \mu \left(\frac{\partial \bar{u}_i}{\partial x_j} + \frac{\partial \bar{u}_j}{\partial x_i} \right) \quad (3.40)$$

Reynolds stresses and turbulent scalar flux introduce other unknowns, and the equations are not closed (they contain more variables than the equations). To close these equations, it necessary to write the turbulent scalar fluxes and the stress tensor in terms of mean quantity.

An approximation, called turbulence models, to close the equation is necessary.

3.3.2 Eddy viscosity model

It can be noted that energy dissipation and transport of mass, momentum, and energy normal to the streamlines are related to the viscosity. Considering that, is now possible to write the eddy-viscosity for the Reynolds stress:

$$-\overline{\rho u'_i u'_j} = \mu_t \left(\frac{\partial u_i}{\partial x_j} + \frac{\partial u_j}{\partial x_i} \right) - \frac{2}{3} \rho \delta_{ij} k \quad (3.41)$$

This model can provide reasonably good results for many flows, but the hypothesis necessary to build the model are not correct in detail.

A simple turbulence model can be written as function of two main parameter: the kinetic energy k and a length scale L .

Partial differential equation to compute turbulence quantities can be adopted. Turbulence to be described require at least a velocity scale and a length scale, so a model that derives the needed quantities form two equations. The kinetic energy terms that define the velocity scale can be derived as follow:

$$\frac{\partial(\rho k)}{\partial t} + \frac{\partial(\rho \bar{u}_j k)}{\partial x_j} = \frac{\partial}{\partial x_j} \left(\mu \frac{\partial k}{\partial x_j} \right) - \frac{\partial}{\partial x_j} \left(\frac{\rho}{2} \overline{u'_j u'_i u'_i} + \overline{p' u'_j} \right) - \rho \overline{u'_i u'_j} \frac{\partial \bar{u}_i}{\partial x_j} - \mu \frac{\partial^2 \bar{u}_i}{\partial x_j^2} \quad (3.42)$$

The length of scale of the turbulence can be determined noting that the dissipation is needed in the energy equation and in equilibrium turbulent flows in which the rates of production and destruction of turbulence are in near-balance. So, the dissipation ε , the kinetic energy k and the length scale correlation is:

$$\varepsilon \approx \frac{k^{3/2}}{L} \quad (3.43)$$

The equation is based on an estimate of the inertial energy transfer: at high Reynolds numbers, there is a cascade of energy form the largest scale to the smallest ones and the energy transferred to the small scales is dissipated.

From the Navier-Stokes's equations, an exact equation for the dissipation can be derived:

$$\frac{\partial(\rho \varepsilon)}{\partial t} + \frac{\partial(\rho u_j \varepsilon)}{\partial x_j} = C_{\varepsilon 1} P_k \frac{\varepsilon}{k} - \rho C_{\varepsilon 2} \frac{\varepsilon^2}{k} + \frac{\partial}{\partial x_j} \left(\frac{\mu_t}{\sigma_\varepsilon} \frac{\partial \varepsilon}{\partial x_j} \right) \quad (3.44)$$

The eddy viscosity in this model is:

$$\mu_t = \rho C_\mu \sqrt{k} L = \rho C_\mu \frac{k^2}{\varepsilon} \quad (3.45)$$

These equations compose the k - ε model, a five parameters model. This model is relatively simple to be implemented in a computer code. RANS equations have the same form as the laminar equation. There is two new differential equation to be solved but, because the time scales associated with the turbulence is much shorter than those connected with the mean flow, so the equations and k - ε model become much stiffer than the laminar flows equation.

So, a difficulty in the discretization of these equations and their resolution, but the solution method must consider an increased stiffness.

3.3.3 RNG k - ε model

For the smallest eddies, the energy dissipation equation can be written as:

$$\frac{\partial(\rho\varepsilon)}{\partial t} + \frac{\partial(\rho u_i \varepsilon)}{\partial x_i} = \frac{\partial}{\partial x_i} \left(\frac{\mu}{Pr_k} \frac{\partial \varepsilon}{\partial x_j} \right) + c_{\varepsilon 3} \rho \varepsilon \frac{\partial u_i}{\partial x_i} + \left(c_{\varepsilon 1} \frac{\partial u_i}{\partial x_j} \tau_{ij} - c_{\varepsilon 2} + c_s S_s \right) \frac{\varepsilon}{k} + S - \rho R \quad (3.46)$$

The equation present two source terms: S is the user-supplied source term and S_s is the term that represents interactions with discrete phase. Pr is the reciprocal ε Prandtl number, μ is the molecular viscosity and $c_{\varepsilon 1}$, $c_{\varepsilon 2}$ and $c_{\varepsilon 3}$ are the model constants. The term R is characteristic for the RNG model and it represent the main difference with the standard one. It can be written as:

$$R = \frac{C_\mu \eta^3 \left(1 - \frac{\eta}{\eta_0}\right) \varepsilon}{(1 + \beta \eta^3) k} \quad (3.47)$$

$$\eta = \frac{k}{\varepsilon} \sqrt{2 S_{ij} S_{ij}} \quad (3.48)$$

$$S_{ij} = \frac{1}{2} \left(\frac{\partial u_i}{\partial x_j} + \frac{\partial u_j}{\partial x_i} \right) \quad (3.49)$$

$$\eta_0 = \left[\frac{C_{\varepsilon 2} - 1}{C_\mu (C_{\varepsilon 1} - 1)} \right]^{\frac{1}{2}} \quad (3.50)$$

The main difference between the standard method and the Re-normalization Group (RNG) methods is about the turbulence length scale considered. RNG can consider different length scale that contribute to the turbulence diffusion [8].

4. Emissions

The mechanism of formation of the pollutant emissions and the influence of the main parameter of the combustion is presented in this chapter. The nature of pollutant formation is such that the concentrations of CO and UHC are highest at low-power conditions and diminish with an increase in power while the NO_x emission attain the maximum values at the highest power condition as shown in Figure 4.1 [3].

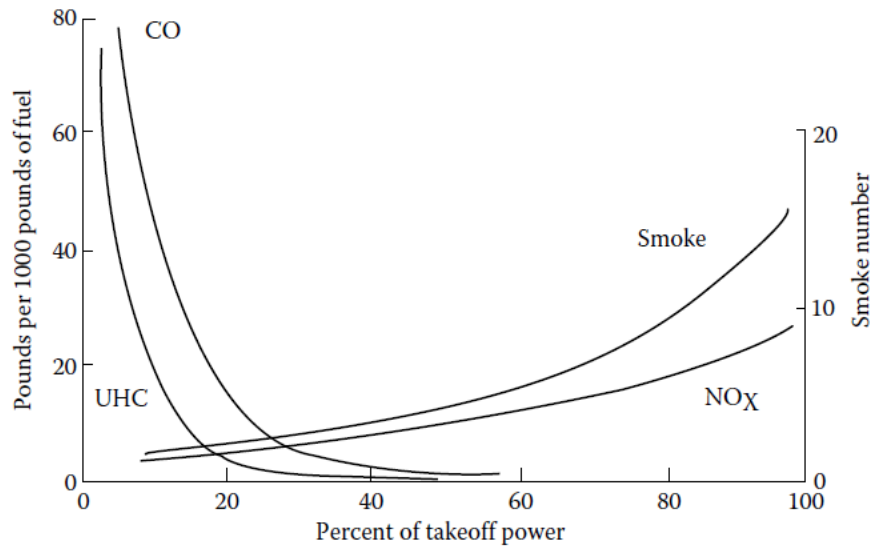


Figure 4.1 Emissions characteristics of gas turbine engines [3]

4.1 Carbon Monoxide

In fuel-rich condition, large amounts of CO are formed due to the low availability of oxygen to complete the reaction to CO₂.

Also, in stoichiometric condition or fuel-lean, the dissociation of CO₂ lead to a significant amount of CO. For this reason, CO emissions are higher than the one predicted from the equilibrium calculations and to be highest at low-power condition with burning rates and peak of temperature relatively low. So, due to the conflict with the equilibrium theory predictions, CO arises from incomplete combustion of the fuel that can be caused by inadequate burning rate in the primary zone, inadequate mixing of the fuel and air that produces some regions in which the mixture strength is too weak to support the combustion and other in which over-rich combustion yields high local concentrations of CO, quenching of the postflame products by entrainment into the liner wall-cooling air.

It can be possible to reduce CO adding additional air downstream to achieve a gradual reduction in burned gas temperature, but CO is quite resistant to oxidation.

At high temperature, the reaction of oxidation can be written as [3]:



While, at low temperature the reaction is:



CO emissions are mainly influenced by the primary-zone equivalence ratio, combustor inlet temperatures and combustion pressure.

The variation of CO emissions with the equivalence ratio is provided by Rink and Lefebvre [9].

Figure 4.2 shows how CO emissions decrease with an increase in the equivalence ratio, with minimum value at 0.8 of equivalence ratio. Above this value, the CO emissions arises. At low levels of the equivalence ratio, the CO emissions arise due to the slow rates of oxidation associated with low combustion temperatures. Increasing the equivalence ratio leads to a rise in the flame temperature that accelerate the reaction of CO oxidation. When the temperature is higher than 1800 K, the CO production rise again due to the CO₂ dissociation.

From Figure 4.2 it can be possible to notice the beneficial effect of an increase in combustion pressure to reduce the CO emissions [3].

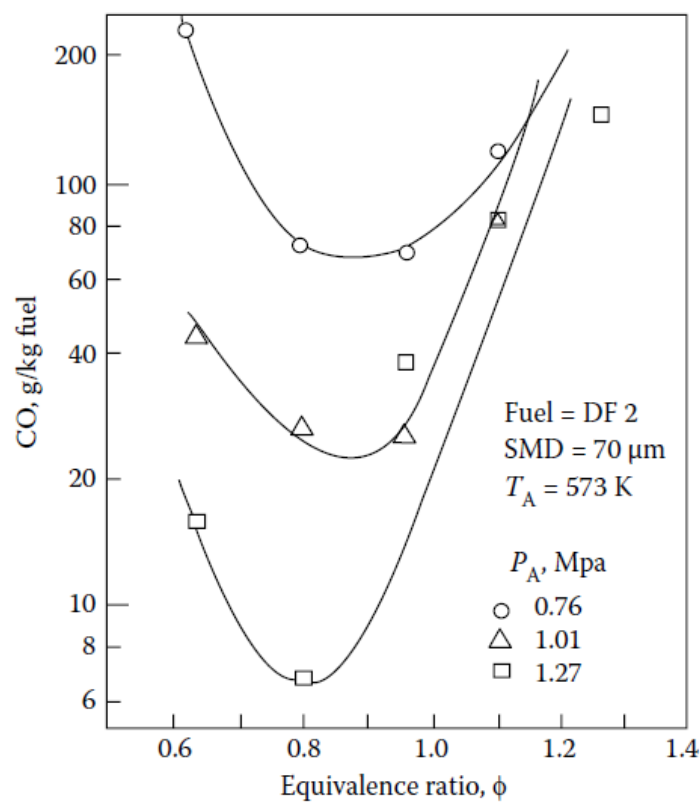


Figure 4.2 Influence of pressure and equivalence ratio on CO. [9]

4.2 Oxides of Nitrogen

It's usual to indicate with NO_x the sum between NO and NO_2 . In fact, most of the nitric oxide formed during the combustion oxide in NO_2 .

There are four different formation mechanism:

- Thermal
- NO oxide mechanism
- Prompt mechanism
- Fuel NO

4.2.1 Thermal Nitric Oxide

Thermal mechanism is referred to the oxidation of atmospheric nitrogen in high-temperature regions of the flame. The process is endothermic, and its rate is significant at temperature around 1850 K.

The reaction scheme usually proposed is the extended Zeldovich mechanism:



The peak of NO formation can be found on the fuel-lean side of stoichiometric, as consequence of the competition between fuel and nitrogen for the oxygen availability. Also, when the combustion temperature is higher on the slightly rich side of stoichiometric, the oxygen available is consumed mainly by the fuel.

The rate of formation and the activation energy required for each reaction imply an exponential dependence of NO_x on flame temperature. The Figure 4.1 show the exponential dependence of thermal NO on the flame temperature. The NO production decrease rapidly with the reduction of temperature, in particular at normal combustor residence time of around 5 ms.

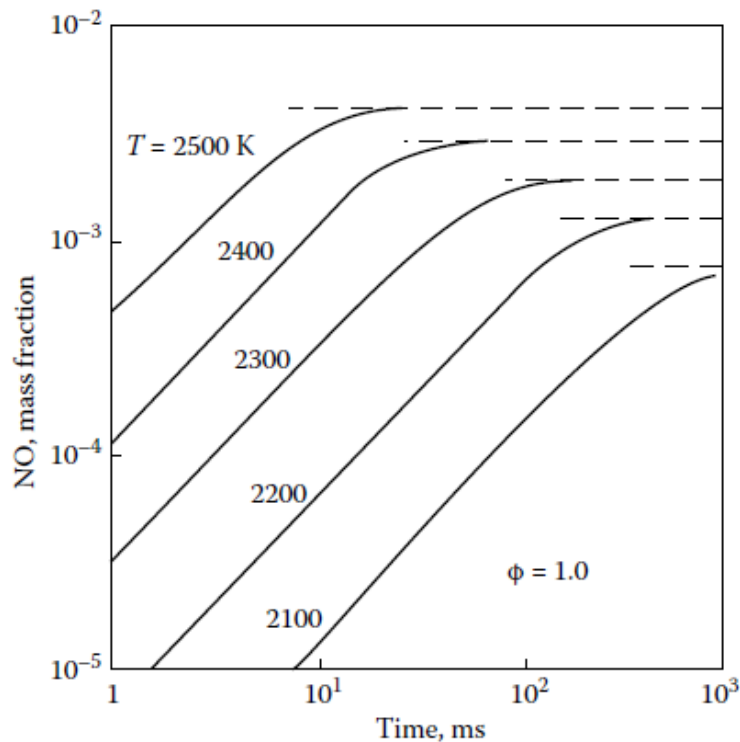


Figure 4.3 NO_x formation as a function of time and temperature; Pa=1 MPa.

This mechanism is mainly influenced by:

- Inlet Air temperature
- Residence time

NO emissions are very dependent of flame temperature, so an increase in inlet air temperature produces a significant increase in NO, as confirmed by the results shown in Figure 4.4.

Residence time can also influence NO_x emissions, as shown in Figure 4.5 that contains the results obtained by Anderson [11].

Figure shows how the nitrogen oxides increase with an increase in residence time. Only for very lean mixture the rate of formation is so low, and it becomes insensitive to time.

It can be concluded that thermal NO mechanism:

- Is controlled by flame temperature.
- Little NO is formed at temperature below 1850 K.
- NO increases linearly with time
- For very lean-premixed combustors, NO formation is largely independent of residence time.

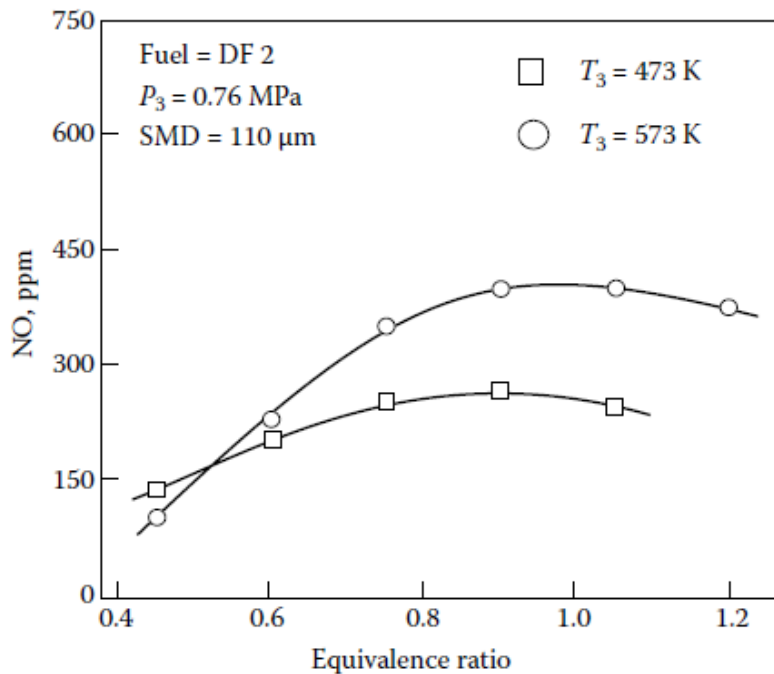


Figure 4.4 Influence of inlet air temperature on NO_x formation [10].

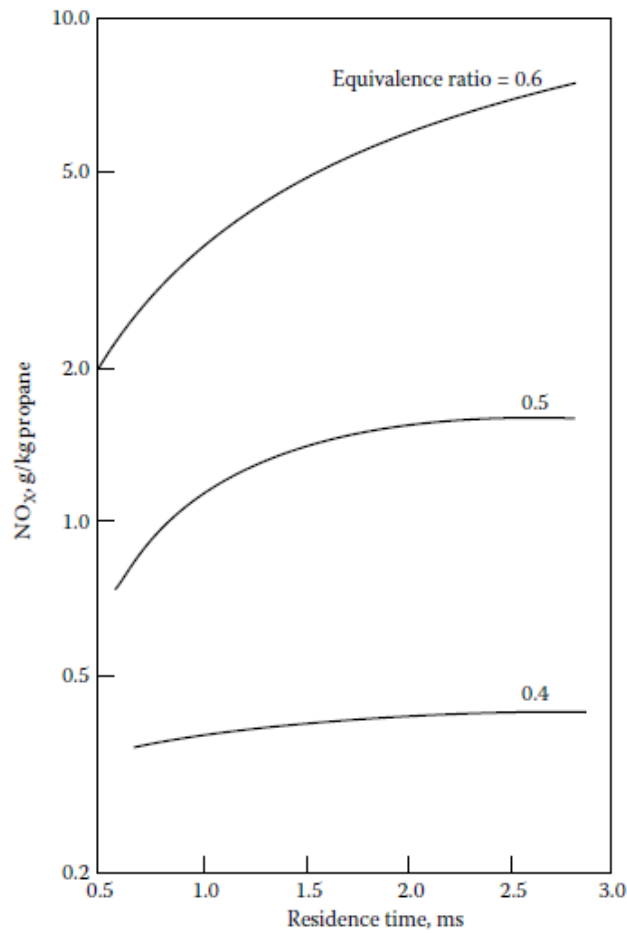


Figure 4.5 Effect of residence time on NO_x in a premixed fuel–air system [11].

4.2.2 Nitrous oxide Mechanism

This mechanism is initiated by the reaction:



And the nitrous oxide formed is then oxidized to NO mainly by the reaction (due to the minor activation energy required):



But also, by:



Further information about this mechanism can be found in Nicol et al. [12]

4.2.3 Prompt Nitric Oxide

NO can be found very early in the flame region. The initiating reactions of this process, according to Nicol et al [12], is:



Prompt mechanisms involve the oxidation of the *HCN* molecules and *N* atoms. The *N* atoms reacts mainly by the second Zeldovich mechanism, while the *HCN* oxides to *NO* following a series of reactions that involve the *HCN* molecules.

4.2.4 Fuel Nitric Oxide

During combustion some of the organically bonded nitrogen contained in the fuel reacts to form the “Fuel *NO*”. This fraction slowly increases with the flame temperature. Natural gases contain little or no fuel bounded nitrogen (FBN). Depending on the degree of nitrogen conversion, fuel *NO* can represent a considerable proportion of the total *NO*.

4.2.5 Influence of Pressure on Oxides of Nitrogen Formation

To lower the fuel consumption of the engine, higher pressure ratio is needed. So, it is important to take into consideration the pressure effects on *NO_x* formation.

For conventional combustor, the *NO_x* depends by the pressure following the formula $NO_x \propto P^n$, where *n* values ranging from 0.5 to 0.8.

Maughan et al results [13] shows how the higher *NO_x* value depends mainly to the thermal mechanism, which exhibits a pressure square-root dependency. Those results are fully consistent with Correa et al works [14],[15]. Figure 4.6 shows some experimental data from Correa et al.

The figure highlights how the *NO_x* formation is independent of pressure in leanest premixed flame. When the flame temperature increases, at higher equivalence ratio, the pressure exponent increase and it attains the value to 0.5 in near-stoichiometric region.

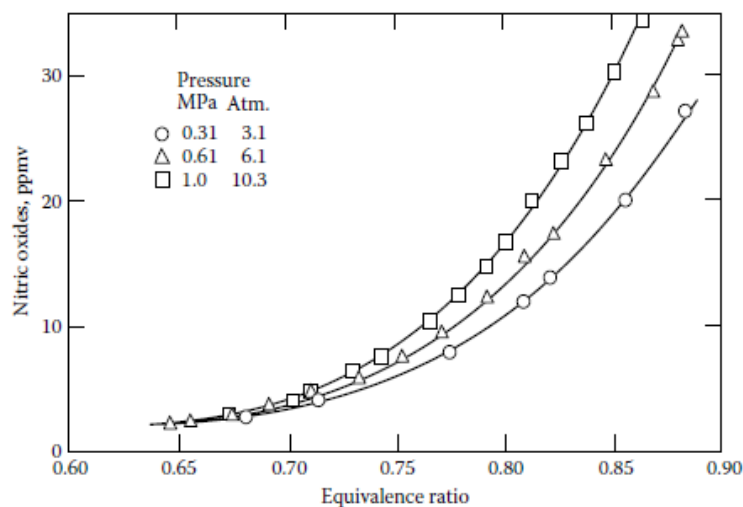


Figure 4.6 Data illustrating the effect of pressure on *NO_x* formation [15].

4.3 Water injection

Different methods are proposed for reducing the gaseous emissions, among them the NO_x is especially highlighted. These methods can be classified into two types: external and internal. The most common internal ways of reducing the gas turbines emissions are the water or steam injection [16].

The water injection has two main effects [17],[18]:

- Thermal effect
- Chemical effect

The thermal effect is related to water action as a diluent of the flame. At a given equivalence ratio, the heat capacity of the mixture increases due to the addition of water and consequently the flame temperature decreases. Water is more effective than steam, due to heat required for the water evaporation.

The temperature at the outlet responses to the water to fuel increasing is a linear decrease.

By introducing water, a linear decrease of the temperature with the

As secondary effect, the addition of water increases the concentrations of important intermediate species in the flame change. Due to changes in the O, H and OH radical concentrations alterations in the reaction pathways might be possible and can affect the emissions formation process, but this effect is of a minor importance compared to the temperature reduction effect and can be neglected.

The water addition slows the rate of the first reaction of the Zeldovich mechanism (main responsible of the NO_x formation) due to lowering in temperature.

However, only if the water evaporates completely before combustion the actual flame temperature can be reduced. If the evaporation process takes too long, only a share of water mass flow participates directly in the combustion reaction while the rest is transported downstream and will not participate. So, as showed in the experimental results an increase of NO_x concentrations in the exhaust gas can be related to an increase in flame temperature and a reduced efficiency of water injection due to a global maldistribution of water in the combustion chamber or due to changes in size distribution of water droplets [17].

The water injection effectiveness in reducing the flame temperature and the effect on lowering the NO_x emissions is also confirmed in the CFD analysis of Shahpouri et al. [19].

From that study the water seems to be more effective than the steam due to latent heat of vaporization needed to evaporate the water. However, for high value of the water to fuel ratio the flame quenched, and this means a CO emissions increase.

From Farokhipour et al., a study of the water injector position optimization can be found [20]

In the Sharafodini et al. numerical study the water is injected with the fuel, as in TG – 20 combustor, achieving a significant reduction on the NO_x. [21]

5. Computational methods for fluid dynamics

The flows and phenomena discussed can be modelled by using partial differential equation. One of the main issues is that the equation cannot be solved in an analytic way and for this reason is necessary to produce an approximate solution with a numerical approach.

Computational fluid dynamics field presents all the methods and algorithms necessary to discretize the equation obtaining an approximate solution by mean of a computer and a commercial code.

The main components necessary are [6]:

- **Mathematical model** that is the set of equations that describe the flow. For each application will be choose the appropriate model, including all the simplifications.
- **Discretization method** once the model is written, the discretization method will give an approximation of the equation. There are different approaches, the main are: finite difference, finite elements, and finite volume.
- **Coordinate and basis vector system** define how the conservation equations will be written since those will depend on which system will be choose.
- **Numerical grid** the geometric domain is described by a subdomain called numerical grid. To divide the main domain there are several options that will be defined by the problem under study.
- **Finite approximation** defined the grid, the following step is to set the approximation for the discretization. In a finite volume method, i.e., is necessary to define the approximation of the surface and volume integrals. This choice will influence the accuracy of the approximation. To be mentioned that higher will be the accuracy, higher will be the number of nodes involved and so bigger is the system to be solved that means an increasing in computational time needed. Thus, one must find a compromise between the computational cost and accuracy using a coarse grid or a locally coarse grid. CONVERGE is a powerful instrument in this field proposing a strategy called AMR (automatic mesh refinement).
- **Solution method** at this point a large system of non-linear algebraic equations is ready to be solved. The non-linearity of the equations requires an iteration scheme to solve the system.
- **Convergence** a method is convergent when the solution tends to the exact solution as the grid spacing tends to zero. The convergence can be checked by using a set of experimental data.
- **Conservation** the set of equations is a conservation law system, so the amount of conserved quantity entering in a control volume has equal to the one that leaves, at the steady state and in absence of source/sink. This condition, i.e. in finite volume, as to be guaranteed for each volume of the domain. Also, the presence of a source/sink as to be consistent, thus the total source/since must be equal to the total flux of the conserved quantities through the boundary.
- **Accuracy** as stated before, the solution given is an approximate solution, so several errors will be introduced and affect the solution. There are mainly three errors: modelling errors that is the difference between the real flows and the one modelled, discretization errors as the difference between the exact solution and the one obtained from the discretizing of the equations, iteration errors introduce by the iterative solution of the equations (also called convergence errors).

The most common used discretization method in 3D CFD is the finite volume method.

5.1 Finite volume methods

The finite volume methods consider the solution domain divided in control volumes subdomain. For each of those volumes that can be called cells, it is possible to define a point at the centre called node.

The method considers the integral conservation equation, then the integral is approximated using a numerical scheme of integration (like the midpoint rule, i.e.).

Finite volume methods conserve the transported quantities both for regular and irregular shaped cells, as main advantage.

A three cells computational domain is now considered in order to understand how the method works and which are the inputs [8].

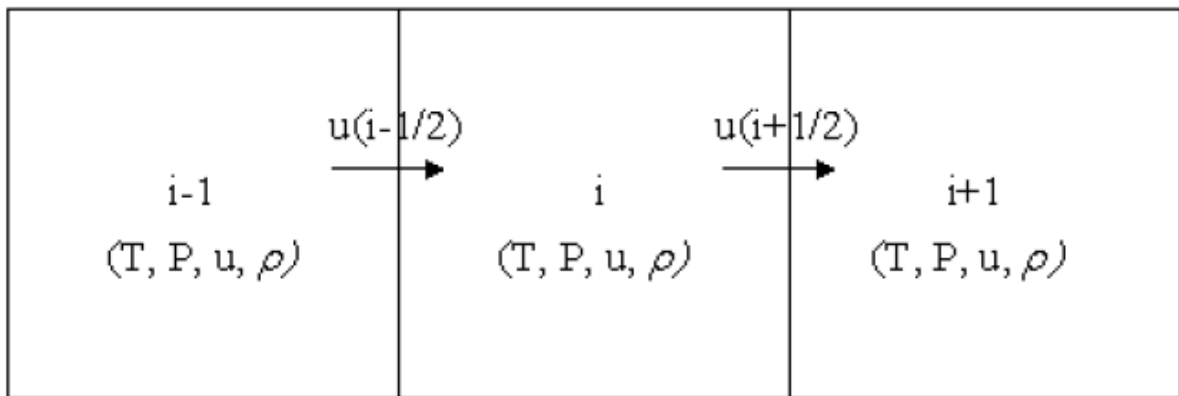


Figure 5.1 Sample three-cell, one-dimensional spatial domain[8].

Let us now consider the transport equation:

$$\frac{\partial \phi}{\partial t} + \frac{\partial u \phi}{\partial x} = 0 \quad (5.1)$$

That in integral form can be written as

$$\frac{d}{dt} \int_V \phi dV + \int_V u \cdot n \phi dS = 0 \quad (5.2)$$

V is the volume of the cell, ϕ the generic flux through this cell, S the surface of the volume with n its normal.

Obtained the integral form, the method sums the fluxes on each face of the cell.

For this reason, it's necessary to interpolate the velocity and flux ϕ to the cell surface. One way to do this is to average the two adjacent cell values and place them on the surface.

This strategy will give a surface ϕ defined as

$$\phi_{i+1/2} = \frac{1}{2} \phi_i + \frac{1}{2} \phi_{i+1} \quad (5.3)$$

and

$$\phi_{i-1/2} = \frac{1}{2} \phi_i + \frac{1}{2} \phi_{i-1} \quad (5.4)$$

Another method can be the Upwind method, that results as

$$\phi_{i+1/2} = \phi_i \quad (5.5)$$

$$\phi_{i-1/2} = \phi_{i-1} \quad (5.6)$$

From each Control Volume can be defined an algebraic equation. The volume integrals are calculated in the same way for every CV, but fluxes at the boundary of the domain need another treatment. These specific fluxes must be known or can be a combination of interior values and boundary data.

The inflow boundary is usually given for convective fluxes. They are zero at impermeable walls and symmetry planes and it can be assumed that are independent of the coordinate normal to the outflow boundary; is that the case where the upwinding can be suitable.

For a diffusive flux are sometimes specified at a wall heat flux or boundary values of variables are prescribed [8].

5.1.1 PISO algorithm

PISO (Pressure Implicit with Splitting of Operators) method is used to the pressure-velocity coupling in CONVERGE. The method starting point, as implemented in CONVERGE, is a predictor step where the momentum equation is solved. After this, a pressure equation is derived and solved, which leads to a correction, which is applied to momentum equation.

This correcting momentum equation process can be repeated as many times as necessary to achieve a certain accuracy.

PISO method can be used both for compressible and incompressible flows. Moreover, allows a semi-implicit treatment of sources and sink (updated at each corrector step) [8].

5.1.2 Solution procedure

Let's consider how CONVERGE solves the transport equations, useful to configure the simulation parameter in the correct way.

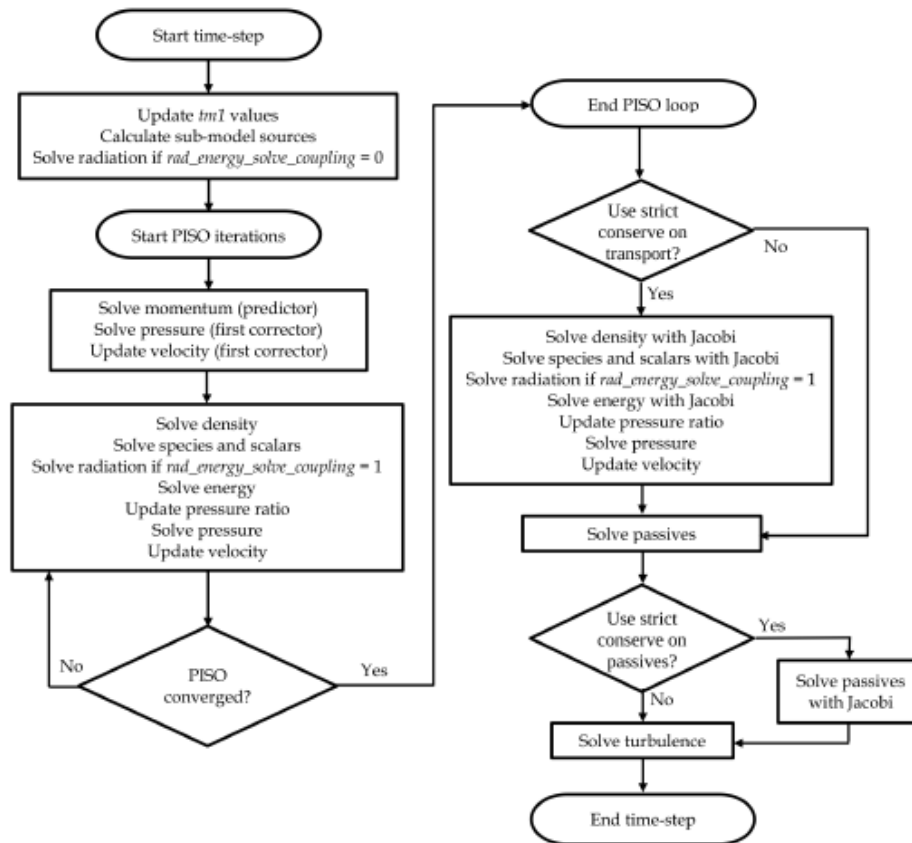


Figure 5.2 Solution order of the transport equations [8].

At the start of each time step, the previous values are stored for all transported quantities. Then, explicit sources are calculated for each sub-model that is currently activated and radiation is solved. At the beginning of the PISO loop, CONVERGE solves for momentum and pressure that sets the velocity for each transport equation. After each PISO iteration, is necessary to check for PISO loop convergence.

For compressible cases, CONVERGE considers that PISO loop to be converged if:

$$\Delta\rho < tol_piso \quad (5.7)$$

So, the density error must be minor than a tolerance.

For incompressible cases, CONVERGE considers PISO loop to be converged when:

$$\Delta P < tol_piso \quad (5.8)$$

Where ΔP is the pressure correction error.

5.1.3 MUSCL

CONVERGE include also different spatial discretization methods for convective term. The convective flux schemes allow to control flux limiters to maintain stability. One of those schemes is the MUSCL (Monotonic Upstream-centered Scheme for Conservation Laws).

This scheme proposed by Van Ler provides a second-order spatial accuracy for the convective term. A scalar ϕ at a cell facing is calculated using a blend of second-order upwind and reconstructed central difference spatial discretization schemes [8].

5.2 Mesh generation

Grid choices affect several aspects of a CFD simulation: accuracy, reliability of the results and the computational effort of the simulation. A finer grid can give more accuracy but as drawback the computational cost will increase. The grid generation depends on the geometry and the phenomena that are under study.

A finer mesh could be applied near the swirler, in example, where the flow is deviated, while the rest of geometry remain coarse.

CONVERGE is a powerful instrument in this field: the grid is automatically generated at each runtime.

The software uses a Cartesian grid generation method: the geometry surface is inside a Cartesian block, the cells will be cut at the surface intersection and after that the intersection information such as normal vector, surface areas will be reduced and stored in each cell. In this way, surface intersections are represented simpler.

When the software finds a cut-cell with a volume less than the 30% of the adjacent cell, the cells are paired. This process is called cell pairing. The center of the cell is now positioned at the volumetric center of the combined two and the transport quantities are shared.

The automatic grid generation consists in trimming the boundary cells, refining the embedding areas and the removing the refinement from the embedding. For a stationary surface, like as the gas turbine combustor subject of this study, the process is performed at the simulation start and every time the geometry is refined or coarsened.

CONVERGE includes several tools for controlling the grid size before and during the simulation. Grid scaling coarsens and refines the base grid size. Fixed embedding refines the grid at specified locations and times. Adaptive Mesh Refinement (AMR) automatically changes the grid based on fluctuating and moving conditions [8].

5.2.1 Grid scaling

Grid scaling can reduce runtimes by coarsening the grid during non-critical simulation times and refining the grid when critical flow phenomena occur.

The base grid size dx_{base} is changed according to:

$$dx_{scaled} = dx_{base} / 2^{grid_scale} \quad (5.9)$$

where $grid_scale$ is the scaling factor and dx_scaled is the new base grid size. If the $grid_scale$ value is 0 the base cells size is unchanged. A positive value will refine the mesh, while a negative one will coarsen it.

5.2.2 Fixed embedding

Fixed embedding tool refines the grid in specific locations of the domain, where a higher resolution is mandatory to increase the accuracy of the solution.

To minimize the simulation time, the rest of the grid remains coarse.

The fixed embedding is based on the following equation:

$$dx_embedded = dx_base / 2^{embedded_scale} \quad (5.10)$$

where $dx_embedded$ is the final value of the cell size, and $embedded_scale$ is the scaling factor of the base cell size dimension.

A further reduction of the computational time can be achieved by specifying the time period when the embedding is applied.

Different fixed embedding strategies are possible:

- Boundary embedding
- Sphere embedding
- Cylinder embedding
- Nozzle and injector embedding
- Box embedding
- Region embedding

5.2.3 Adaptive mesh refinement (AMR)

Adaptive mesh refinement automatically refines the grid based on fluctuating and moving conditions such as temperature and velocity. It can be useful to simulate complex phenomena such as flame propagation or high-velocity flow accurately thanks to a highly refined grid and without affecting the overall simulation time with a globally refined grid.

A good adaptive mesh refinement algorithm will add higher grid resolution (embedding) where the flow field is most under-resolved or where the sub-grid field is the largest (i.e., where the curvature [gradient] of a specified field variable is the highest).

For a scalar, the sub-grid field is defined as the difference between the actual field and the resolved field:

$$\phi' = \phi - \bar{\phi} \quad (5.11)$$

where ϕ is the actual scalar field, $\bar{\phi}$ is the resolved scalar field, and ϕ' is the sub-grid scalar field. The sub-grid for any scalar can be expressed as an infinite series. From this series, considering that it is not possible to take into consideration all the series, only the first term is taken into account:

$$\phi' \cong -\alpha_{[k]} \frac{\partial^2 \bar{\phi}}{\partial x_k \partial x_k} \quad (5.12)$$

AMR can be enabled for any or as many of the following field: velocity, number of parcels per cell, temperature, void fraction, species, passives, or boundary. For each condition, a different embedding scale and different sub-grid criterion can be specified. It can be also specified the time when the AMR will start and when it will end for each field.

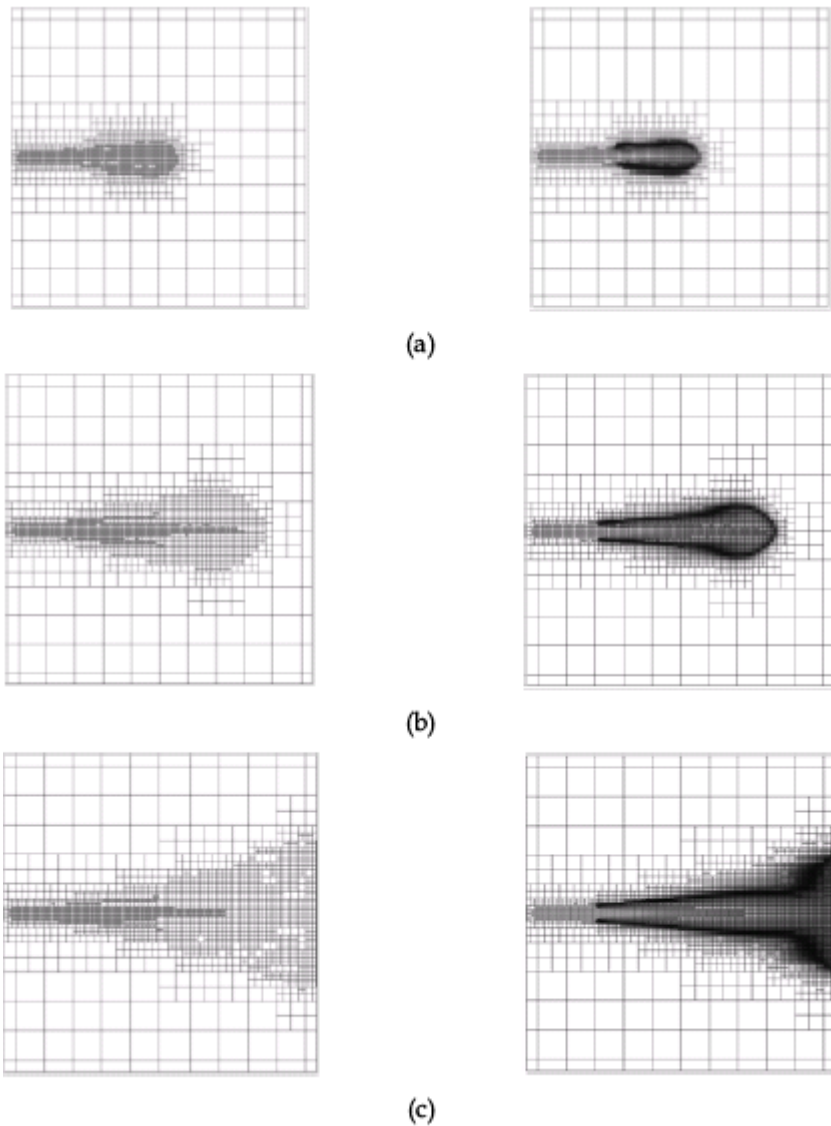


Figure 5.3 Evolution of a combustive spray bomb. The grid was generated by AMR in a sequence of time steps after the start of the simulation. Right column- Grid only. Left column Grid and temperature values (Black means T=2800 K cca) [8]

6. TG – 20 model, case setup and results

6.1 TG – 20 geometry model

The first step of every 3D CFD simulation is the creation of a geometry model. The TG – 20 model is characterized by:

- The casing which takes the air given by the compressor and then recirculate this air inside the burner. The air condition inside the casing is supposed equal to the outlet air of compressor.
- The burner that presents 7 rings of cooling channel, 8 mixing holes and 3 series of dilution holes: the first two composed by 6 holes and last one by 4 holes starting from the injector to the head end of the combustor. The air that come from the casing is distributed inside those holes due to the diameter differences of the holes, and thanks to the pressure gradient.

The first series of holes, that are called primary and secondary cooling holes, collect the air that will mix with fuel starting the combustion inside the burner.

The last series of holes receive the air not needed for the combustion or for the wall cooling. This air lowers the fluid temperature to avoid damage to the turbine blade. The air that flow through the cooling channels must also reduce the burner surface temperature, avoiding creep that can cause the burner failure. (Figure 6.1)

- The methane is injected through 8 holes with a spray angle of 30° (Figure 6.2).
- An air-swirler with 26 blades that ensure a certain turbulence to the fluid, to have a good mixing and sustain the combustion. A small gap between swirler and burner is present to cool the swirler (Figure 6.3).

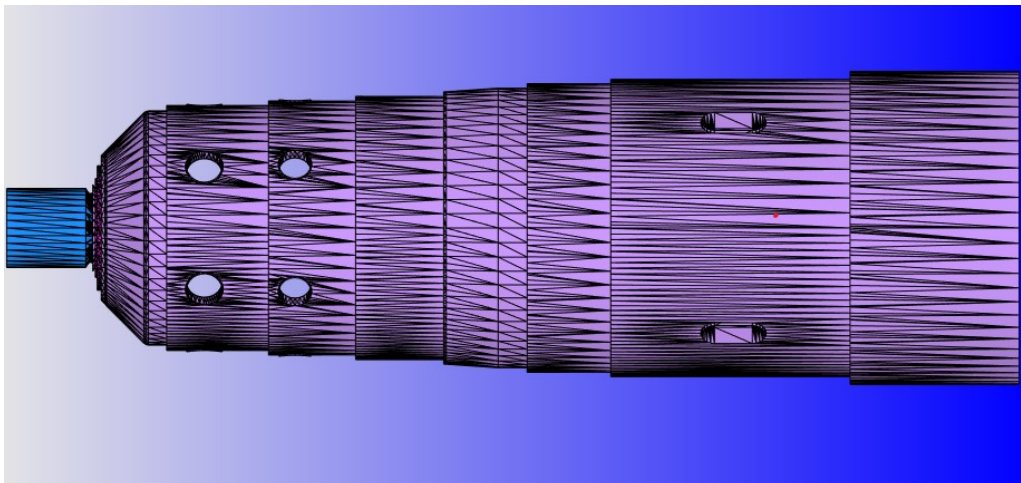


Figure 6.1 TG - 20 combustor view of primary, secondary and dilution holes

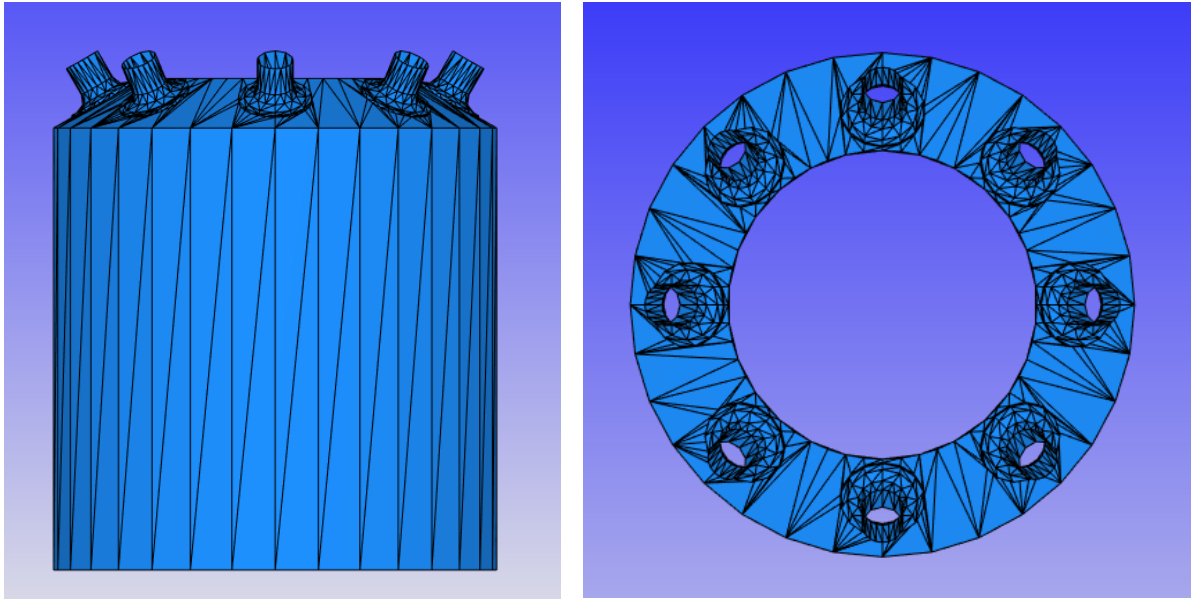


Figure 6.2 Front and up view of the injectors

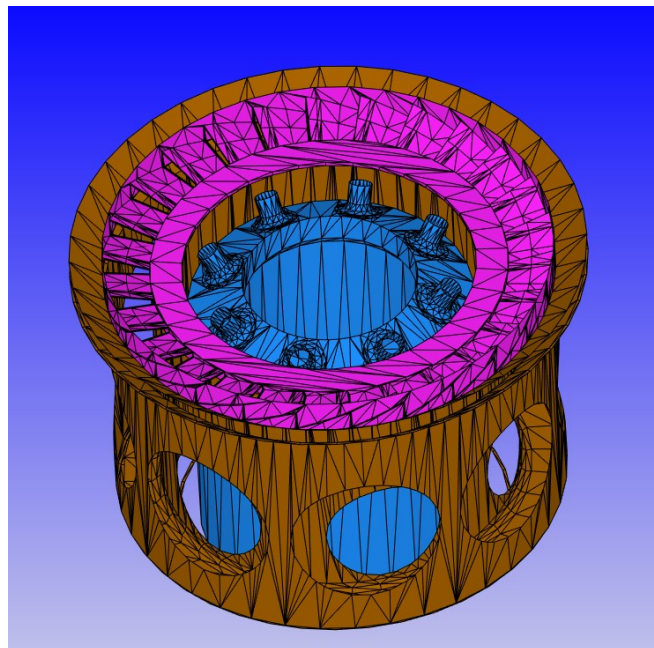


Figure 6.3 View of the injectors and the air-swirler

6.2 Dry Case

The simulation results obtained for the two different dry case setups are here discussed. For both the simulation the inflow mass inside the casing air is 17,46 m/s, the methane injected is 0,27125 m/s at an initial temperature of 306 K. The initial air temperature has been set at 651 K and 1,1012 MPa. Those parameters have been set from experimental data provided by Ethos Energy coming from the Duino plant.

The numerical setup and the mesh definition are resumed in Table 1.

The combustion model chosen for both the simulation is the FGM but using two different reaction mechanism: the GRI-mech and CRECK mechanism. The first one is composed by 53 species and 325 reactions, the second one includes 53 species and 2459 reactions so much more detailed than the GRI-mech.

Table 1 Grid definition and main numerical setup of the two simulation

| Mesh | | |
|-------------------|-------------------|-----------------------------------|
| Base grid [mm] | 4*4*4 | 4*4*4 |
| Minimum dimension | 0,625 by AMR | 0,625 by AMR |
| Numerical setup | | |
| Solver | Steady state | Steady state |
| | PISO | PISO MUSCL |
| Combustion model | FGM | FGM |
| | GRI-mech | CRECK mech |
| Turbulence model | RNG k- ϵ | RNG k- ϵ |
| | Std wall function | non- equilibrium wall function |

To improve the accuracy of the simulation, the second order MUSCL scheme is introduced. The turbulence model adopted is the RNG k- ϵ model with a different wall function for the two cases. The wall function allows to the software to make an assumption about the viscous sublayer. The standard wall function assumes the law-of-wall for velocity in log-law region so the turbulence near the wall is not dependent from the wall conditions far from it. The non-equilibrium wall function assumes that the cells near the wall have a velocity profile comprised of a viscous sublayer and log-law turbulent layer.

Figure 6.4 and Figure 6.5 shows the mean temperature and the pressure profile inside the combustor. The pressure is quasi-constant during all the cycles of the simulation, a minor variation of this quantity is obtained in the CRECK simulation. The mean temperature reaches almost the same value at the steady state.

From Figure 6.6 and Figure 6.7 is possible to evaluate the temperature distribution inside the combustor on the YZ and XZ plan, respectively. This distribution presents a more symmetric behaviour in the CRECK simulation. It can be possible to appreciate the primary recirculation zone where the toroidal structure of the fluid provides air to the fuel starting the combustion. The temperature is lowered by the presence of the dilution holes in order to preserve the turbine blades.

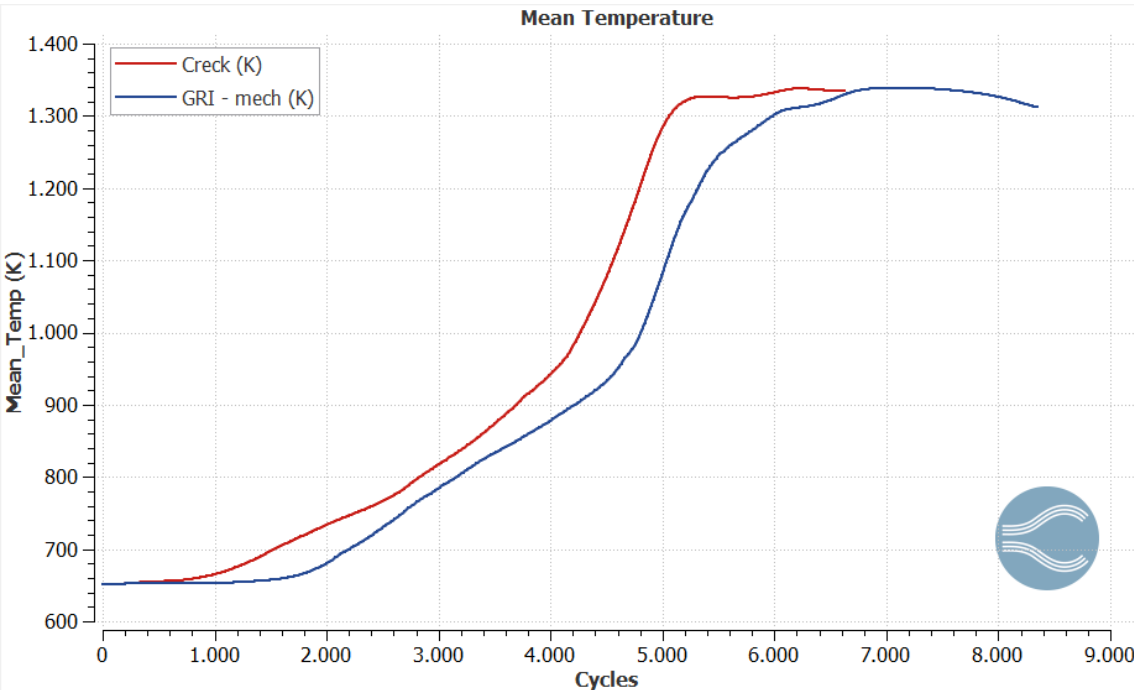


Figure 6.4 Mean temperature comparison: GRI-mech (blu) and Creck (ed)

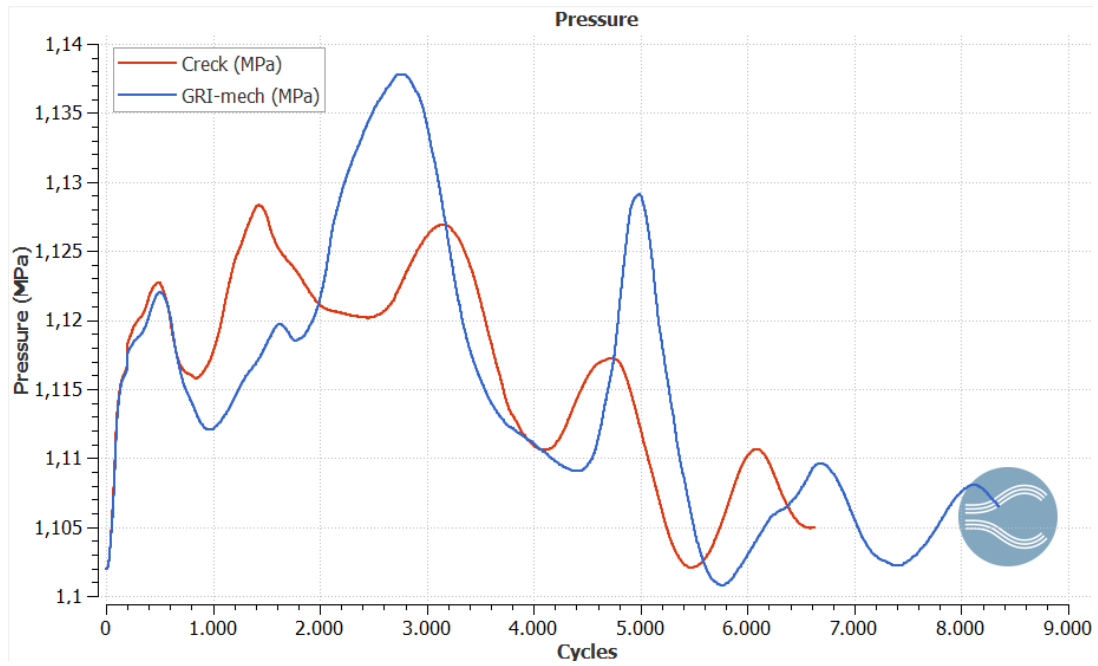


Figure 6.5 Mean pressure comparison: GRI-mech (blue) and Creck (red)

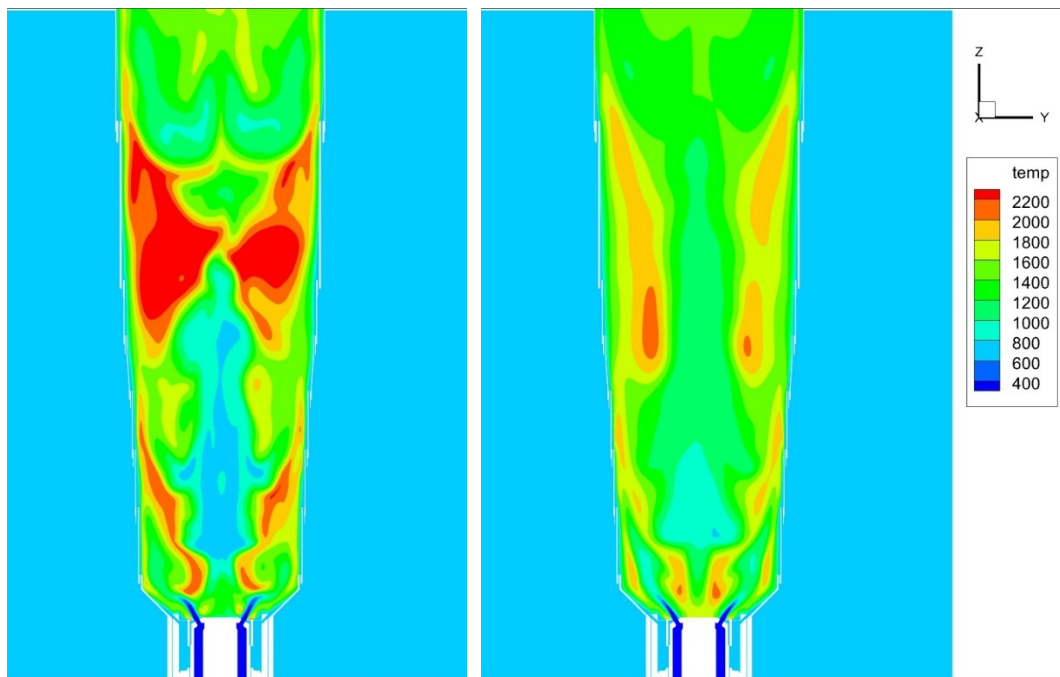


Figure 6.6 Temperature distribution comparison (YZ plan): GRI-Mech (left) and Creck (right)

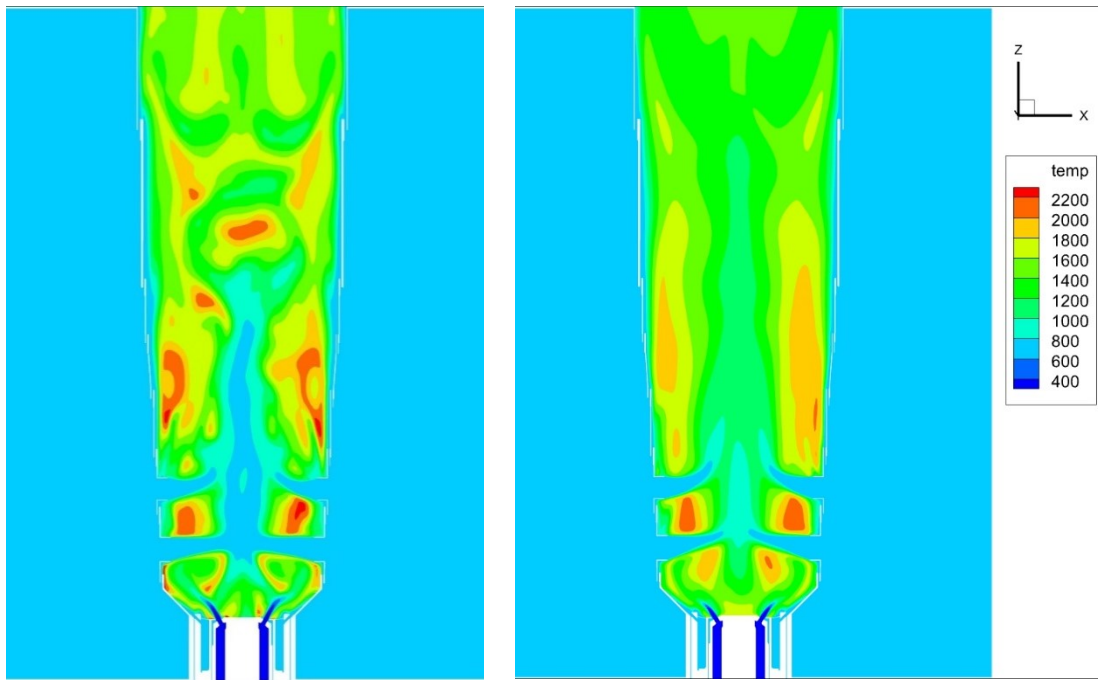


Figure 6.7 Temperature distribution comparison (XZ plane): GRI-Mech (left) and Creck (right)

The Turbulence Kinetic Energy and Turbulence Dissipation Rate are analysed in Figure 6.8 and Figure 6.9. A higher turbulence characterized the CRECK simulation. This turbulence condition leads to a better mixing of the air and fuel. In fact, from the velocity vectors (Figure 6.10 and Figure 6.11) the primary recirculation zone results more extended in the CRECK simulation.

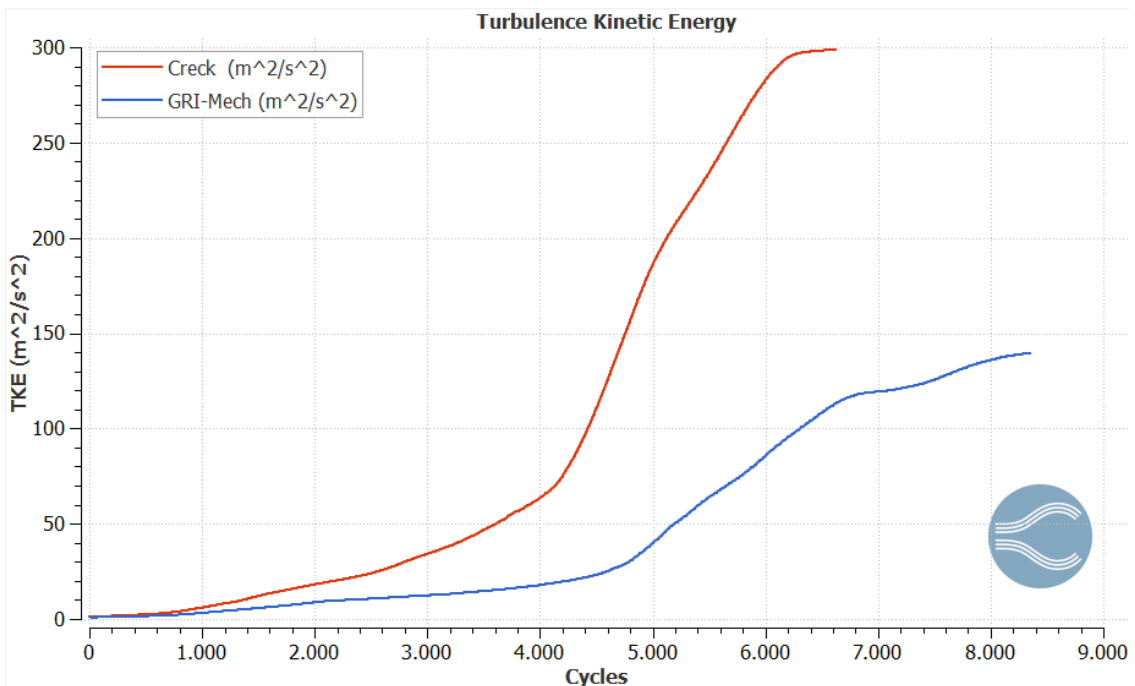


Figure 6.8 Turbulence Kinetic Energy comparison: GRI-mech (blue) and Creck (red)

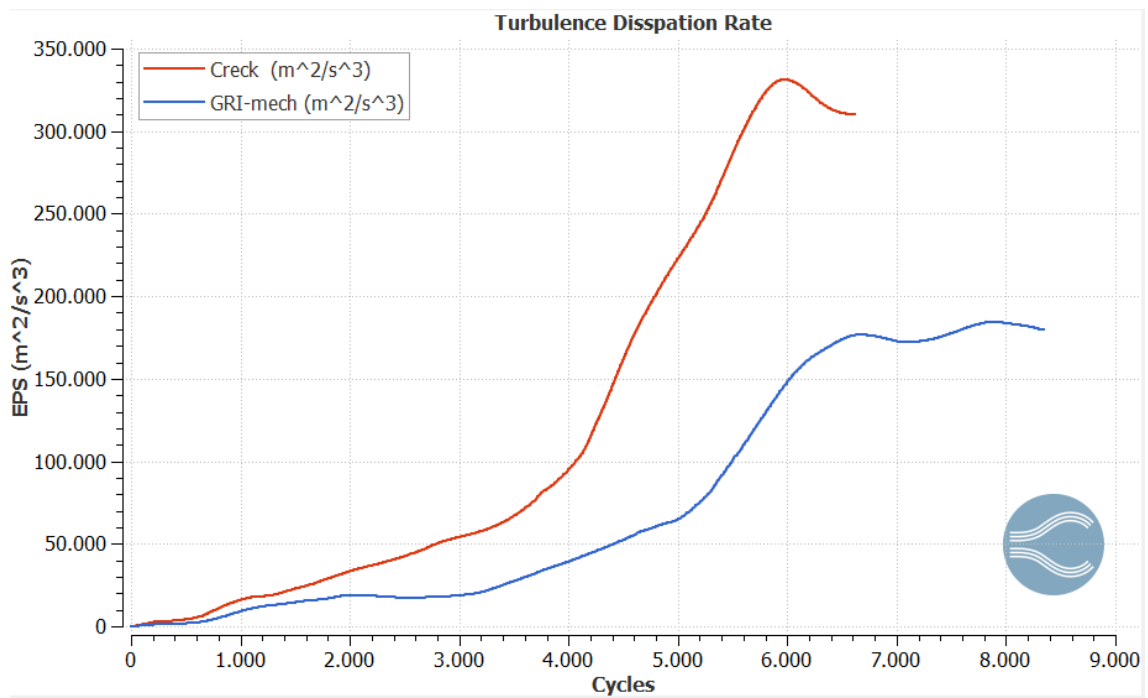


Figure 6.9 Turbulence Dissipation Rate comparison: GRI-mech (blue) and Creck (red)

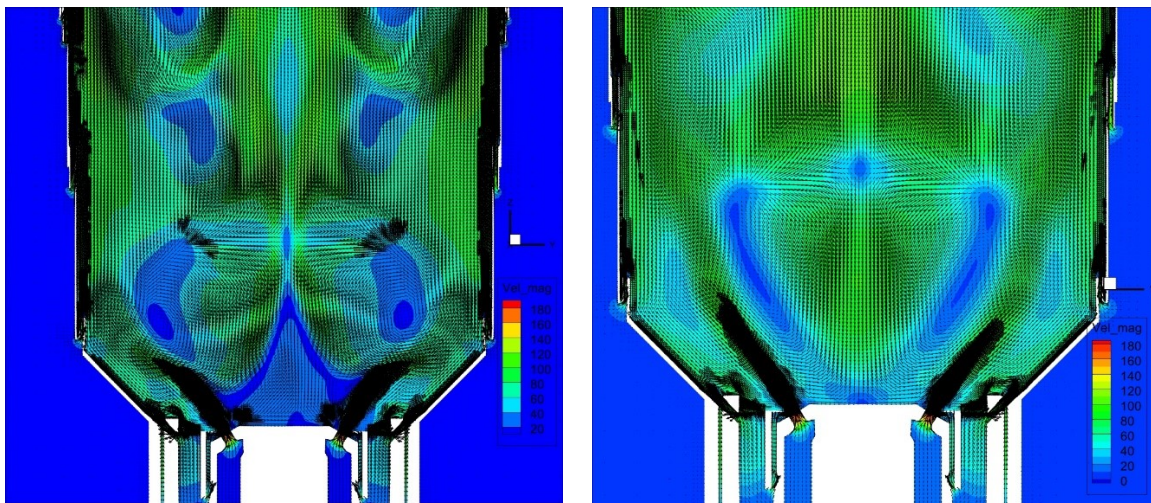


Figure 6.10 Velocity magnitude and velocity vectors comparison in the primary recirculation zone (YZ plan): GRI-mech (left) and Creck (right)

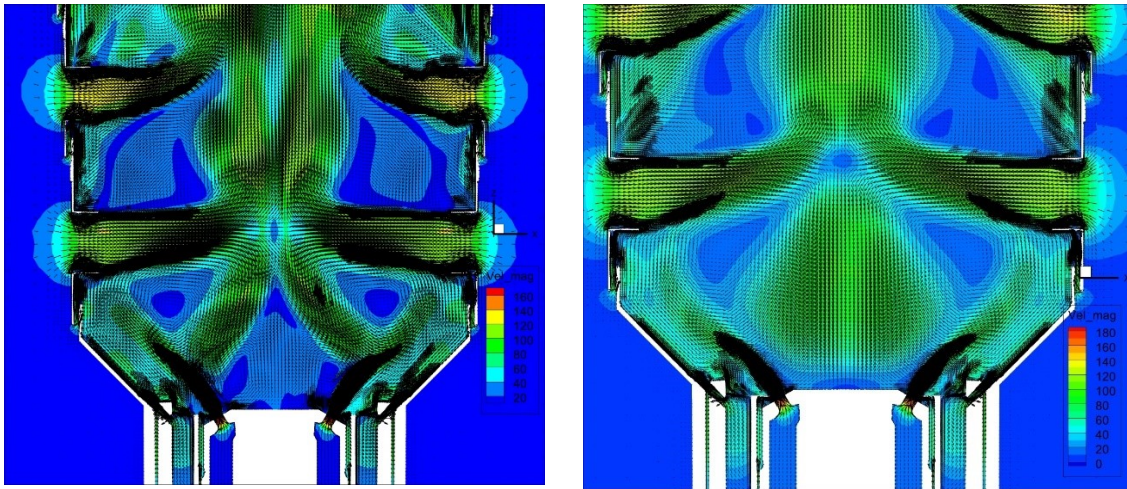


Figure 6.11 Velocity magnitude and velocity vectors comparison in the primary recirculation zone (XZ plan): GRI-mech (left) and Creck (right)

Figure 6.12 and Figure 6.13 presents the equivalence ratio on the YZ and XZ plan. It can be possible to see the toroidal reverse flow in the primary zone induced by the primary cooling holes and the swirler vane angle. This toroidal flow guarantees a continuous ignition of the mixture. The symmetric behaviour of the equivalence ratio obtained in the CRECK simulation is consistent with the temperature profile previously analysed.

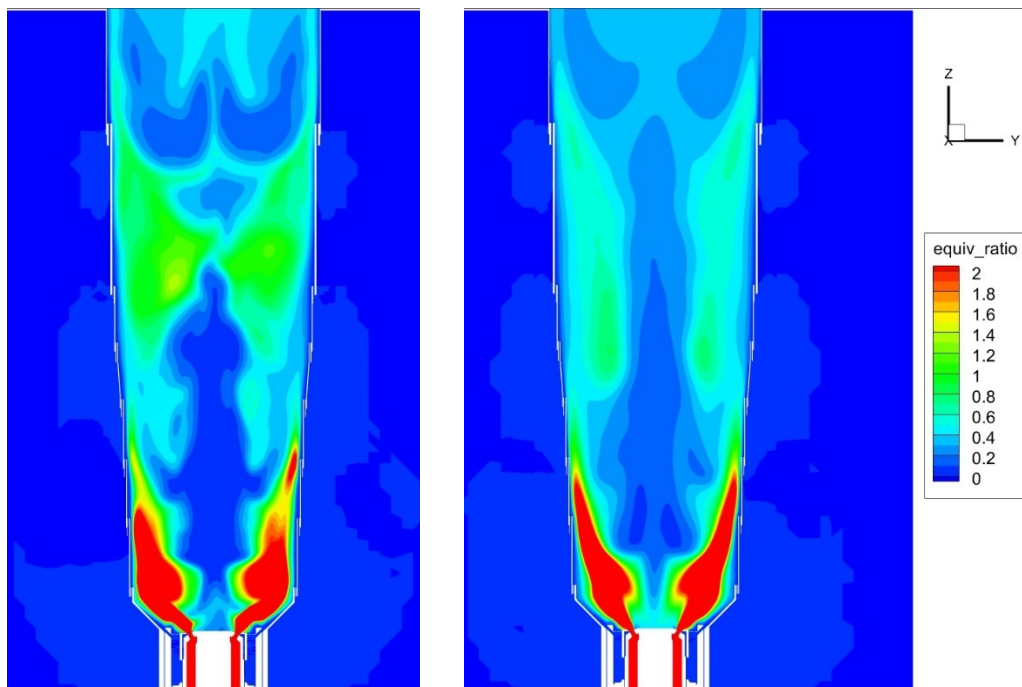


Figure 6.12 Equivalence ratio comparison (YZ Plan): GRI-mech (left) and Creck (right)

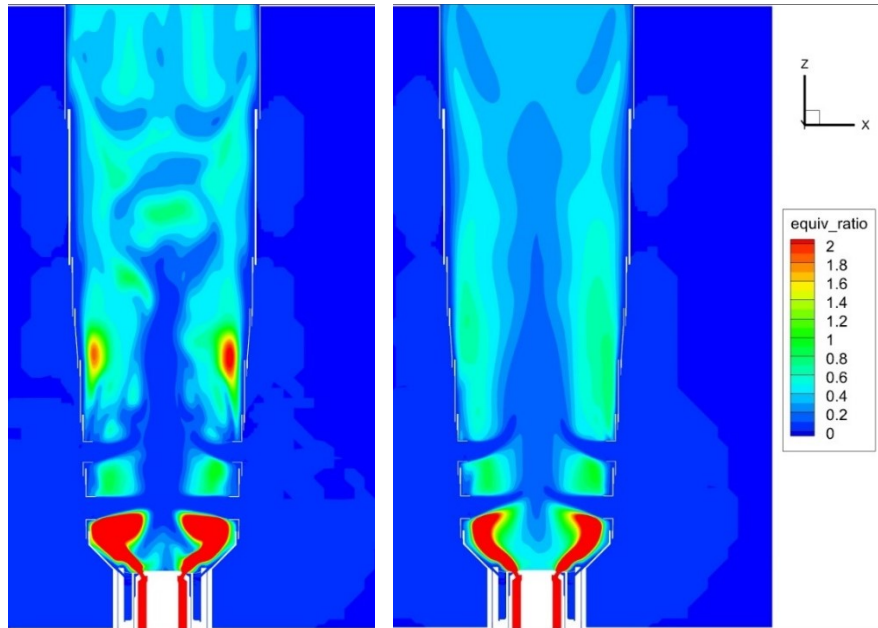


Figure 6.13 Equivalence ratio comparison (XZ Plan): GRI-mech (left) and Creck (right)

The CO emissions are highly related with the equivalence ratio. The CO distribution and are showed in Figure 6.14, Figure 6.15 shows the profile at the outlet of the combustor. The highest CO concentration can be found in the primary recirculation zone where we have the fuel rich zone. Most of the CO product in this region, is than oxide in the intermediate zone using additional air. Figure 6.16 shows the final concentration of CO at the outlet of the combustor.

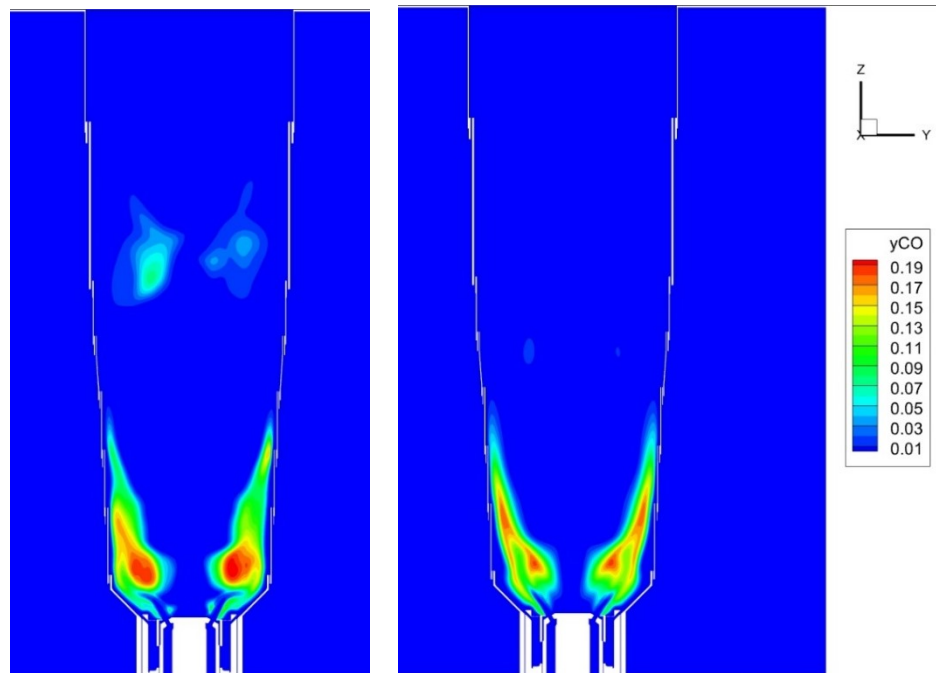


Figure 6.14 CO distribution (YZ Plan): GRI-mech(left) and Creck (right)

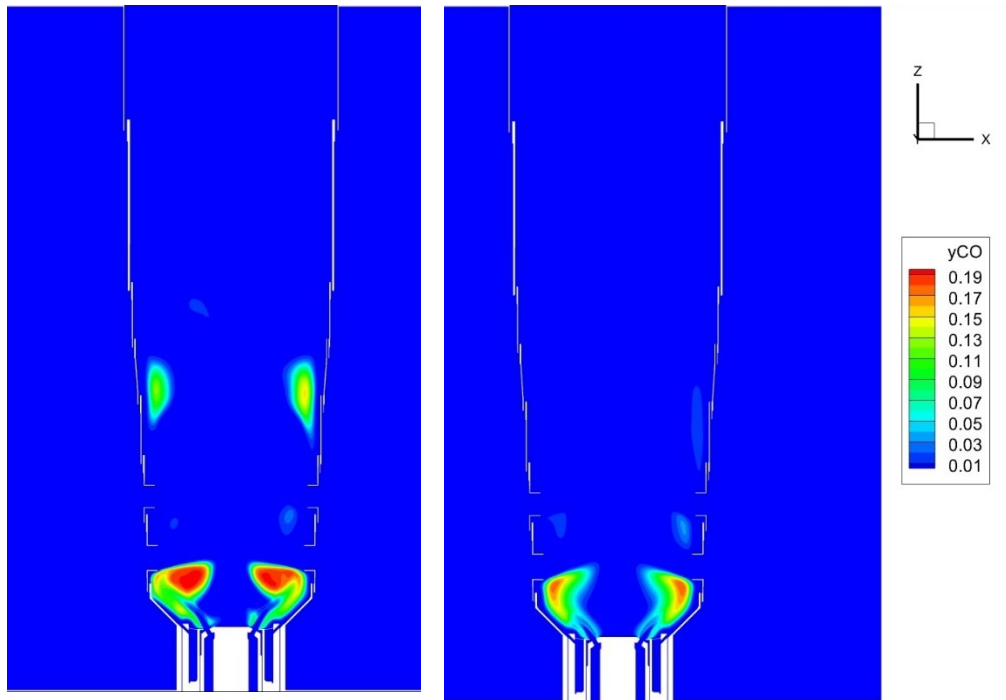


Figure 6.15 CO distribution (XZ Plan): GRI-mech(left) and Creck (right)

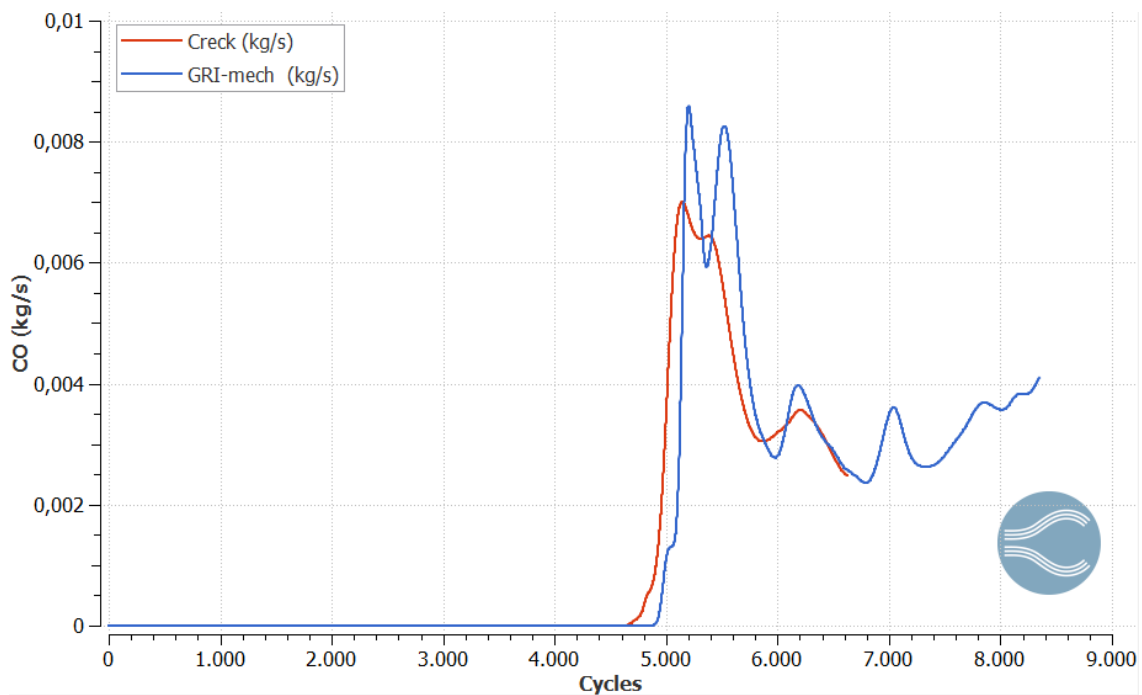


Figure 6.16 CO emissions at the outlet comparison: GRI-mech (blue) and Creck (red)

NO_x emissions, represented in Figure 6.17 and Figure 6.18, follow the temperature profile due to the thermal formation mechanism that is the main responsible of the NO_x production. Figure 6.19 shows the NO_x emissions profile at the turbine outlet.

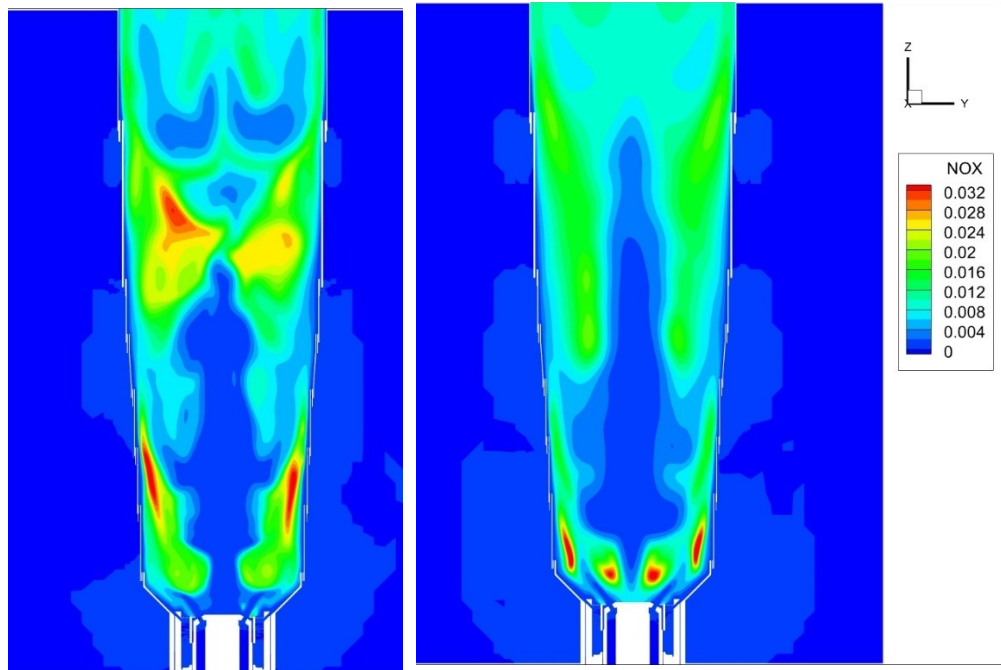


Figure 6.17 NO_x distribution (YZ Plan): GRI-mech (left) and Creck (right)

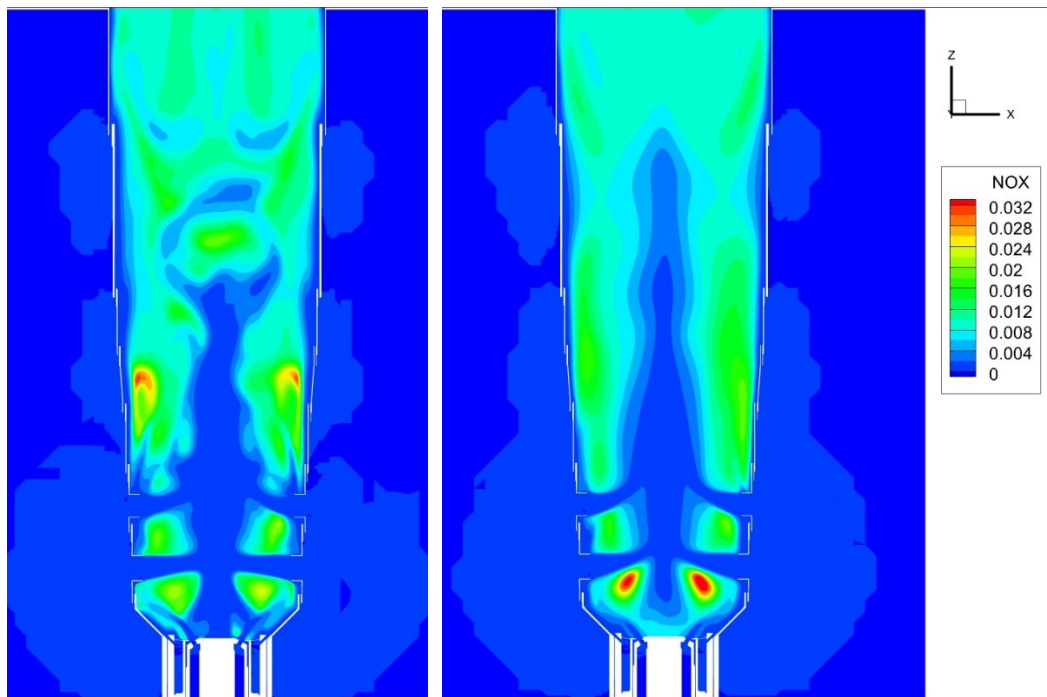


Figure 6.18 NO_x distribution (XZ plan): GRI-mech (left) and Creck (right)

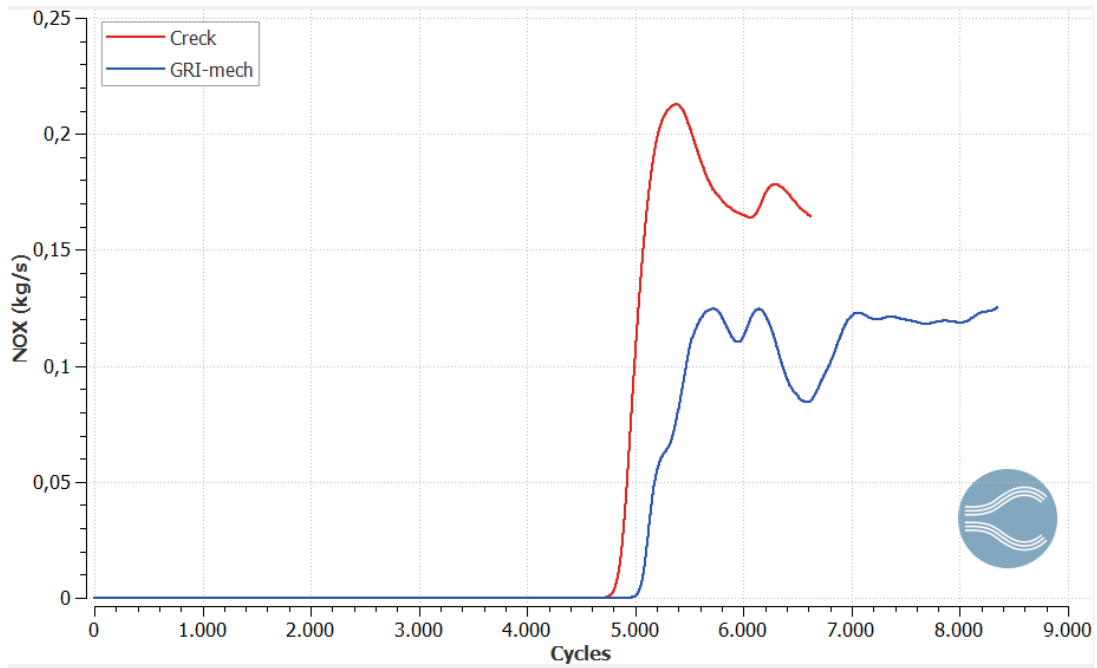


Figure 6.19 NO_x emissions at the outlet comparison: GRI-mech (blue) and Creck (red)

The higher fraction of UHC is mainly composed by CH₄. The quantity of the unburned methane at the combustor outlet is plotted in Figure 6.20. The CRECK simulation presents a reduction of two order of magnitude, thanks to the higher turbulence and better mixing obtained in this model.

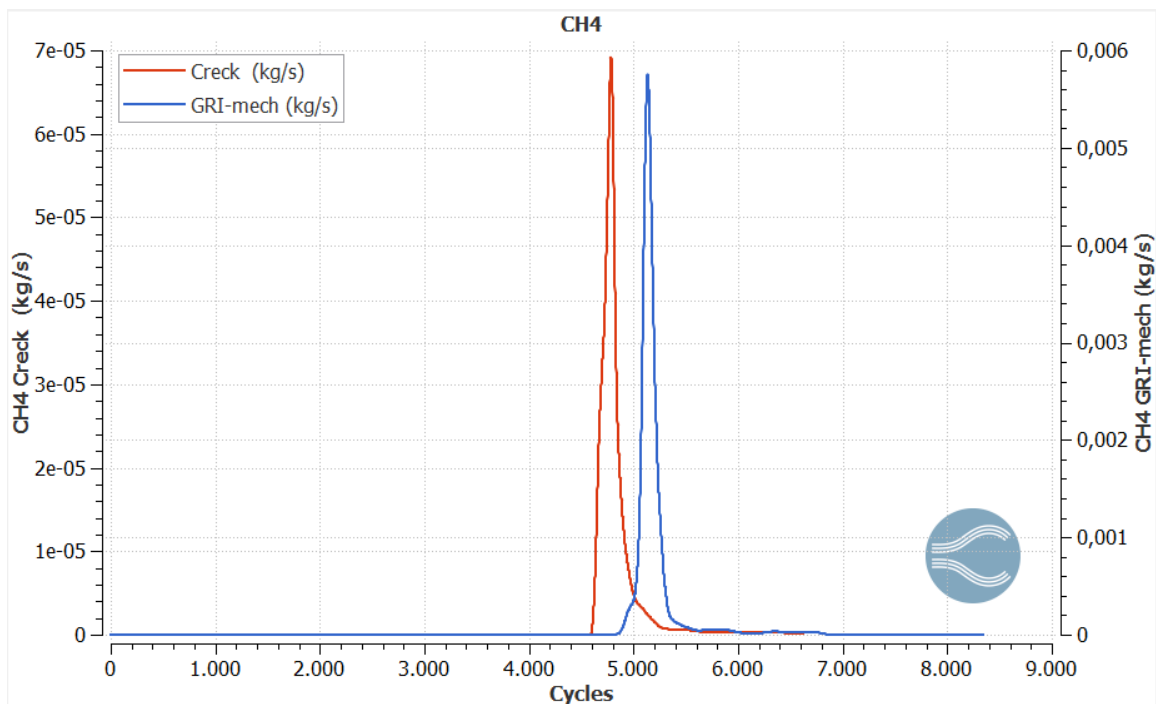


Figure 6.20 CH₄ emissions at the outlet: GRI-mech (left) and Creck (red)

6.3 Preliminary study

The water evaporation inside the burner can be modelled simpler introducing 8 heat sinks (one for each injector), avoiding the computational effort required for a VOF simulation but preserving the accuracy of the model.

The water is introduced inside the combustor using the same line and injector of the fuel.

A two-phase flow inside a pipe, like the injector, is dictated by various competing forces as shear stress, capillarity, gravity, and momentum. Also, horizontal two-phase flow is more complex than vertical due to the gravity. Due to high velocity assumed by the gas, the flow pattern can be assumed annular. So, the liquid forms a continuous film around the perimeter of the tube wall and gas flows as a central core. [22]

It can be concluded that the spray injection can be modelled as a hollow spray injection.

To understand how to model the heat sink, a preliminary study of the water injection has been conducted in a simplified geometry.

This simplified geometry is obtained by the NASA-LDI turbine substituting the injector with one with the same geometry of the TG – 20. The inlet air is at the same pressure of 11,02 bar and temperature of 651,15 K of the heavy-duty gas turbine.

The swirler of this turbine will approximately reproduce the flow shape as in the real turbine combustor.

The geometry of NASA-LDI is showed in Figure 6.21.

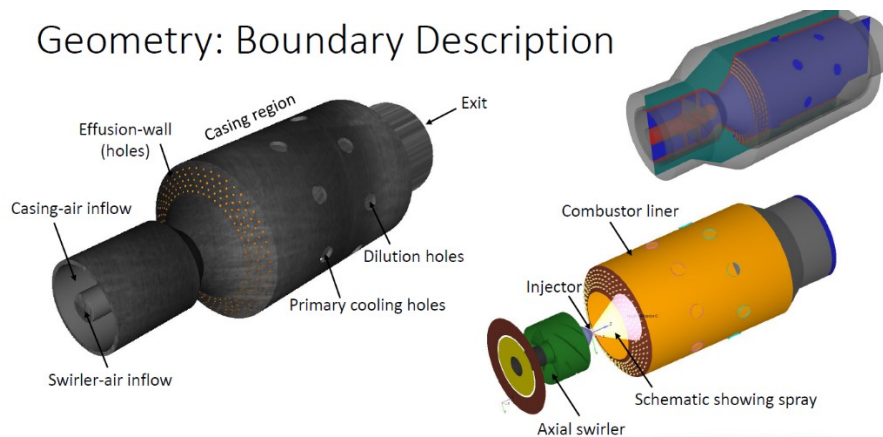


Figure 6.21 NASA LDI gas turbine geometry and boundary

In order to reproduce the same conditions between the TG – 20 and the NASA LDI combustor, due to the different geometry of the two combustors, a first simulation without water injection has been set to define the mass flow rate at the combustor outlet. The results obtained is of 0,278 kg/s.

So, the amount of water that must be injected in the NASA LDI combustor to achieve the same condition as in TG – 20 is:

$$\dot{m}_{H_2O,LDI} = \dot{m}_3 \left(1 + \frac{1}{\alpha} + \frac{0,32}{\alpha} \right) * (y_{H_2O}) = 1,39E - 3 \text{ kg/s} \quad (6.1)$$

Where the water concentration y_{H_2O} is obtained from the TG - 20 at 0,32 water to fuel ratio as:

$$y_{H_2O} = \frac{\dot{m}_{H_2O}}{\dot{m}_{air} + \dot{m}_{fuel} + \dot{m}_{H_2O}} \quad (6.2)$$

The heat subtracted by the sink and considering the Mollier diagram the evaporation take place at constant pressure. The water is at same temperature of 300 K as the fuel and reaches the saturation temperature of 458,8 K at the pressure of 11,4 bar.

So, the power subtracted inside the combustor by evaporation can be defined as the difference between the vapor saturation level and liquid saturation:

$$Q_{vap} = h_N - h_L = 2670,04 \text{ kJ/kg} \quad (6.3)$$

By multiplying the water mass flow rate to heat required for the evaporation, it can be defined the power subtracted by the sink due to the evaporation of the water inside the combustor.

The sink modelled in this way assumes that the water enters inside the combustor already in vapour at a temperature of 300 K. The sink is placed downstream the injector wall replicating the subtracting of heat from the surrounding air.

To validate the sink model, this one is compared with the results coming from the simulation with the water injection. Since there are no experimental data about the water distribution inside the combustor, three model are taken consideration:

- Blob droplet distribution
- Rosin-Rammler distribution
- Chi-squared distribution

In all the simulation, in order to achieve fast results in short time and since the main interest is the heat subtracted by the water evaporation, the combustion is not simulated.

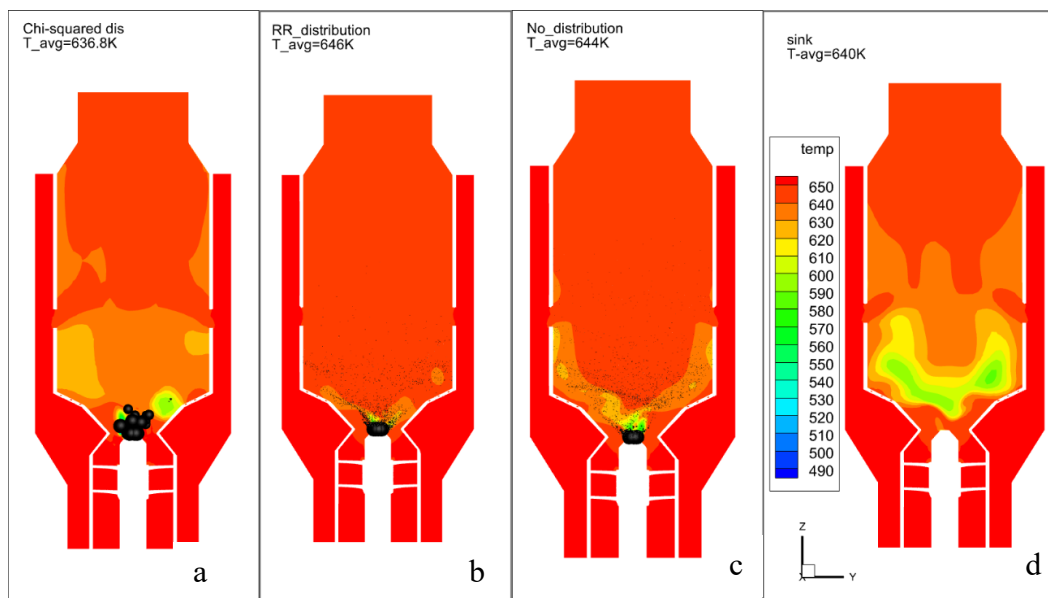


Figure 6.22 Parcel distribution and temperature profile comparison a) Chi-squared distribution b) Rosin-Rammler distribution c) Blob droplet distribution d) heat sink

The Figure 6.22 shows the results of the simulations. The temperature average obtained in the model with heat sink is similar to the one with the water injection. The temperature average variation of ± 6 K between the heat sink model and the others can be observed. So, this study confirms that the water evaporation modelled as a simple heat sink is quite accurate and has the same impact on the mean temperature as the water injection model.

7. Conclusions and future directions

In this work, two different dry model has been studied. The main difference between the two model consists in the reaction mechanism adopted, the wall treatment and the implementation of a second order spatial scheme in order to improve the accuracy of the model. The initial model presents the GRI-mech mechanism and a standard wall function, the new model implements the MUSCL second order scheme, the more detailed CRECK reaction mechanism and an enhanced wall function. The mesh strategy is the same for both the model and turbulence model is the RANS RNG k- ϵ .

The new model shows a symmetry in temperature with the direct consequence of a symmetric distribution of the emissions.

This symmetry allows to make some geometrical simplification of the TG – 20 model. Due to this symmetry, the combustor geometry can be halved using a periodic boundary condition. In this way, the computational effort can be reduced.

Also, to improve the accuracy of the model a recalibration of the turbulence and the NO_x model can be taken in consideration.

A preliminary study on a simplified geometry has been also conducted. The temperature distribution obtained from the water injection model and heat sink model validate this simplified model.

The heat sink model can be implemented and optimized in the TG – 20 model, studying the reduction of the NO_x and comparing the results with the experimental one and the literature. Also, the effect of the water to fuel ratio on NO_x emissions can be obtained from this model.

8. Figure index

| | |
|---|----|
| 0FIGURE 1.1 GLOBAL ENERGY DEMAND AND CO ₂ EMISSIONS TRENDS IN THE STATED POLICIES SCENARIO, 2019-2030..... | 1 |
| FIGURE 2.1 T-S DIAGRAM OF A JOULE-BRAYTON CYCLE [2] | 3 |
| FIGURE 2.2 THE THREE MAIN COMBUSTOR TYPES [3]..... | 4 |
| FIGURE 2.3 TWO BASIC TYPES OF ANNULAR DIFFUSERS: (A) AERODYNAMIC, (B) DUMP. [3] | 6 |
| FIGURE 2.4 MAIN COMPONENTS OF A CONVENTIONAL COMBUSTOR [3]..... | 6 |
| FIGURE 3.1 SCHEMATIC REPRESENTATION OF A TURBULENT MOTION (LEFT) AND THE TIME DEPENDENCE OF A VELOCITY COMPONENT AT A POINT (RIGHT) [6]..... | 16 |
| FIGURE 3.2 TIME AVERAGING FOR A STATISTICALLY STEADY FLOW (LEFT) AND ENSEMBLE AVERAGING [6] | 17 |
| FIGURE 4.1 EMISSIONS CHARACTERISTICS OF GAS TURBINE ENGINES [3]..... | 22 |
| FIGURE 4.2 INFLUENCE OF PRESSURE AND EQUIVALENCE RATIO ON CO. [9] | 23 |
| FIGURE 4.3 NO _x FORMATION AS A FUNCTION OF TIME AND TEMPERATURE; P _a =1 MPa. | 24 |
| FIGURE 4.4 INFLUENCE OF INLET AIR TEMPERATURE ON NO _x FORMATION [10]..... | 25 |
| FIGURE 4.5 EFFECT OF RESIDENCE TIME ON NO _x IN A PREMIXED FUEL–AIR SYSTEM [11]. | 26 |
| FIGURE 4.6 DATA ILLUSTRATING THE EFFECT OF PRESSURE ON NO _x FORMATION [15]. | 27 |
| FIGURE 5.1 SAMPLE THREE-CELL, ONE-DIMENSIONAL SPATIAL DOMAIN[8]..... | 30 |
| FIGURE 5.2 SOLUTION ORDER OF THE TRANSPORT EQUATIONS [8]..... | 32 |
| FIGURE 5.3 EVOLUTION OF A COMBUSTING SPRAY BOMB. THE GRID WAS GENERATED BY AMR IN A SEQUENCE OF TIME STEPS AFTER THE START OF THE SIMULATION. RIGHT COLUMN- GRID ONLY. LEFT COLUMN GRID AND TEMPERATURE VALUES (BLACK MEANS T=2800 K CCA) [8] | 35 |
| FIGURE 6.1 TG - 20 COMBUSTOR VIEW OF PRIMARY, SECONDARY AND DILUTION HOLES | 37 |
| FIGURE 6.2 FRONT AND UP VIEW OF THE INJECTORS | 38 |
| FIGURE 6.3 VIEW OF THE INJECTORS AND THE AIR-SWIRLER..... | 38 |
| FIGURE 6.4 MEAN TEMPERATURE COMPARISON: GRI-MECH (BLU) AND CRECK (ED) | 40 |
| FIGURE 6.5 MEAN PRESSURE COMPARISON: GRI-MECH (BLUE) AND CRECK (RED) | 41 |
| FIGURE 6.6 TEMPERATURE DISTRIBUTION COMPARISON (YZ PLAN): GRI-MECH (LEFT) AND CRECK (RIGHT) | 41 |
| FIGURE 6.7 TEMPERATURE DISTRIBUTION COMPARISON (XZ PLANE): GRI-MECH (LEFT) AND CRECK (RIGHT) | 42 |
| FIGURE 6.8 TURBULENCE KINETIC ENERGY COMPARISON: GRI-MECH (BLUE) AND CRECK (RED) | 42 |
| FIGURE 6.9 TURBULENCE DISSIPATION RATE COMPARISON: GRI-MECH (BLUE) AND CRECK (RED)..... | 43 |
| FIGURE 6.10 VELOCITY MAGNITUDE AND VELOCITY VECTORS COMPARISON IN THE PRIMARY RECIRCULATION ZONE (YZ PLAN): GRI-MECH (LEFT) AND CRECK (RIGHT)..... | 43 |

| | |
|---|----|
| FIGURE 6.11 VELOCITY MAGNITUDE AND VELOCITY VECTORS COMPARISON IN THE PRIMARY RECIRCULATION ZONE (XZ PLAN): GRI-MECH (LEFT) AND CRECK (RIGHT)..... | 44 |
| FIGURE 6.12 EQUIVALENCE RATIO COMPARISON (YZ PLAN): GRI-MECH (LEFT) AND CRECK (RIGHT)..... | 44 |
| FIGURE 6.13 EQUIVALENCE RATIO COMPARISON (XZ PLAN): GRI-MECH (LEFT) AND CRECK (RIGHT)..... | 45 |
| FIGURE 6.14 CO DISTRIBUTION (YZ PLAN): GRI-MECH(LEFT) AND CRECK (RIGHT)..... | 45 |
| FIGURE 6.15 CO DISTRIBUTION (XZ PLAN): GRI-MECH(LEFT) AND CRECK (RIGHT)..... | 46 |
| FIGURE 6.16 CO EMISSIONS AT THE OUTLET COMPARISON: GRI-MECH (BLUE) AND CRECK (RED)..... | 46 |
| FIGURE 6.17 NOX DISTRIBUTION (YZ PLAN): GRI-MECH (LEFT) AND CRECK (RIGHT)..... | 47 |
| FIGURE 6.18 NOX DISTRIBUTION (XZ PLAN): GRI-MECH (LEFT) AND CRECK (RIGHT)..... | 47 |
| FIGURE 6.19 NOX EMISSIONS AT THE OUTLET COMPARISON: GRI-MECH (BLUE) AND CRECK (RED)..... | 48 |
| FIGURE 6.20 CH4 EMISSIONS AT THE OUTLET: GRI-MECH (LEFT) AND CRECK (RED)..... | 48 |
| FIGURE 6.21 NASA LDI GAS TURBINE GEOMETRY AND BOUNDARY | 49 |
| FIGURE 6.22 PARCEL DISTRIBUTION AND TEMPERATURE PROFILE COMPARISON A) CHI-SQUARED DISTRIBUTION B) ROSIN-RAMMLER DISTRIBUTION C) BLOB DROPLET DISTRIBUTION D) HEAT SINK..... | 50 |

9. Bibliography

- [1] IEA, Global energy demand and CO₂ emissions trends in the Stated Policies Scenario, 2019-2030
- [2] H. I. H. Saravanamuttoo, G. F. C. Rogers, e H. Cohen, *Gas turbine theory*, Seventh edition. Harlow, England ; New York: Pearson, 2017.
- [3] A. H. Lefebvre e D. R. Ballal, *Gas turbine combustion alternative fuels and emissions*. Boca Raton [u.a.: Taylor & Francis, 2010
- [4] A. Donini, “Advanced Turbulent Combustion Modeling for Gas Turbine Application,” 2014.
- [5] D. C. Wilcox, *Turbulence modeling for CFD*, 3rd ed. La Cãnada, Calif: DCW Industries, 2006.
- [6] J. H. Ferziger e M. Perić, *Computational methods for fluid dynamics*, 3rd, ed ed. Berlin ; New York: Springer, 2002.
- [7] J. BARDINA, J. FERZIGER, and W. REYNOLDS, “Improved subgrid-scale models for large-eddy simulation,” 2013.
- [8] M. S. CONVERGECFD and M. Series, “CONVERGE Manual, CONVERGE CFD 2.4,” no. Sep, 2019.
- [9] Rink, K. K., and Lefebvre, A. H., “Influence of Fuel Drop Size and Combustor Operating Conditions on Pollutant Emissions,” *International Journal of Turbo and Jet Engines*, Vol. 6, No. 2, pp. 113–22, 1989.
- [10] Rink, K. K., and Lefebvre, A. H., “The Influence of Fuel Composition and Spray Characteristics on Nitric Oxide Formation,” *Combustion, Science and Technology*, Vol. 68, pp. 1–14, 1989.
- [11] Anderson, D. N., “Effects of Equivalence Ratio and Dwell Time on Exhaust Emissions from an Experimental Premixing Prevaporizing Burner,” *ASME Paper 75-GT-69*, 1975.
- [12] Nicol, D., Malte, P. C., Lai, J., Marinov, N. N., and Pratt, D. T., “NO_x Sensitivities for Gas Turbine Engines Operated on Lean-Premixed Combustion and Conventional Diffusion Flames,” *ASME Paper 92-GT-115*, 1992.
- [13] Maughan, J. R., Luts, A., and Bautista, P. J., “A Dry Low NO_x Combustor for the MS3002 Regenerative Gas Turbine,” *ASME Paper 94-GT-252*, 1994.
- [14] Correa, S. M., “Lean Premixed Combustion for Gas Turbines: Review and Required Research,” *Fossil Fuel Combustion*, ASME PD-Vol. 33, 1991.

- [15] Leonard, G. L., and Correa, S. M., "NO_x Formation in Lean Premixed High-Pressure Methane Flames," Second ASME Fossil Fuel Combustion Symposium, PD-30, ASME, New York, NY, pp. 69–74, 1990.
- [16] A. Farokhipour, E. Hamidpour, e E. Amani, "A numerical study of NO_x reduction by water spray injection in gas turbine combustion chambers", *Fuel*, vol. 212, pagg. 173–186, gen. 2018, doi: 10.1016/j.fuel.2017.10.033.
- [17] S. Lellek, C. Barfuß, e T. Sattelmayer, "Experimental Study of the Interaction of Water Sprays With Swirling Premixed Natural Gas Flames", giu. 2016, doi: 10.1115/GT2016-56158.
- [18] R. Kollrack e L. D. Aceto, "The Effects of Liquid Water Addition In Gas Turbine Combustors", *Journal of the Air Pollution Control Association*, vol. 23, n. 2, pagg. 116–121, feb. 1973, doi: 10.1080/00022470.1973.10469750.
- [19] S. Shahpouri e E. Houshfar, "Nitrogen oxides reduction and performance enhancement of combustor with direct water injection and humidification of inlet air", *Clean Technologies and Environmental Policy*, vol. 21, n. 3, pagg. 667–683, apr. 2019, doi: 10.1007/s10098-019-01666-4.
- [20] A. Farokhipour, E. Hamidpour, e E. Amani, "A numerical study of NO_x reduction by water spray injection in gas turbine combustion chambers", *Fuel*, vol. 212, pagg. 173–186, gen. 2018, doi: 10.1016/j.fuel.2017.10.033.
- [21] R. Sharafodini, Department of Mechanical Engineering, Tehran Gharb branch, Islamic Azad University, Tehran, Iran, M. R. Habibi, Energy Technologies Research Division, Research Institute of Petroleum Industry (RIPI), Tehran, Iran, M. Pirmohammadi, e Department of Mechanical Engineering, Pardis Branch, Islamic Azad University, Pardis, Iran, "Numerical Study of Water Vapor Injection in the Combustion Chamber to Reduce Gas Turbine Fuel Consumption", *Journal of Applied Fluid Mechanics*, vol. 13, n. 3, pagg. 1047–1054, mag. 2020, doi:10.29252/jafm.13.03.30466.
- [22] Darzi, M, & Park, C. "Experimental Visualization and Numerical Simulation of liquid-Gas Two-Phase Flows in a Horizontal Pipe." Proceedings of the ASME 2017 International Mechanical Engineering Congress and Exposition. Volume 7: Fluids Engineering. Tampa, Florida, USA. November 3–9, 2017. V007T09A011. ASME. doi.org/10.1115/IMECE2017-72113